Underwater Optical Wireless Localization

December 21, 2021

Underwater Optical Wireless Localization

By Ziqi Dou,

A THESIS SUBMITTED TO THE DEPARTMENT OF ELECTRICAL AND
COMPUTER ENGINEERING
AND THE SCHOOL OF GRADUATE STUDIES
OF MCMASTER UNIVERSITY
IN PARTIAL FULFILMENT OF THE REQUIREMENTS
FOR THE DEGREE OF
MASTER OF APPLIED SCIENCE

McMaster University

Master of Applied Science (2021)

Hamilton, Ontario (Department of Electrical and Computer Engineering)

TITLE: Underwater Optical Wireless Localization

AUTHOR: Ziqi Dou (McMaster University)

SUPERVISOR: Dr. Steve Hranilovic

NUMBER OF PAGES: xv, 94

List of Symbols

α Energy scale parameter

γ Spectral peak rise factor

λ Wave length

μ Dynamic viscosity coefficient

ω Angular velocity of wave

ω_m Peak frequency

ω_n Wave circular frequency

ρ Fluid density

θ Direction angle

ε_n Random initial phase

a_n Wave amplitude

c Speed of light in a vacuum

d Depth of water

f Frequency

$G(\omega,\theta)$ Directional distribution function

g Acceleration of gravity

h Planck constant

k Wave number

P Pressure force

r Water particle radius of motion

R_X Receiver

$S(\omega)$ Energy spectrum

t Time

T_X Transmitter

U Wind velocity at 19.5 m above ocean surface

v Fluid velocity vector

List of Acronyms

UAWC Underwater acoustic wireless communications. 2, 12

UWC Underwater Wireless Communication. 1

UWOC Underwater Wireless Optical Communications. 1, 2, 12

UWSNs Underwater Wireless Senor Networks. 2

Abstract

With the development of underwater technology, a more significant number of scholars and scientists have begun to pay attention to the development and application of UWOC (Underwater optical wireless communication) and UWONs (Underwater optical wireless networks). These studies require underwater localization technology to provide accurate location information. This thesis applies existing underwater positioning technology with knowledge of the LED Lambertian pattern with the aim of developing a low latency underwater positioning concept that helps locate the fast-moving underwater targets.

A key contribution of this thesis is the development of an adaptive time slot (ATS) approach. Each buoy transmits signals in disjoint time slots which repeats periodically. Given the random locations and orientations of the buoys, the distance from each buoy to the target will not be identical and will change in time. These changes in position lead to overlap, discontinuity or loss of signals transmitted from buoys in each time slot. The ATS approach use the structure of these distortions received from multiple buoys to improve positioning accuracy. The thesis provides a comparison results with and without ATS in several practical scenarios.

Acknowledgements

First of all, I want to show my deepest gratitude to my supervisor, Dr. Steve Hranilovic. He is a very enthusiastic and positive professor. Whenever a group meeting is held, I feel very enjoy chatting and laughing with the big family of the group. Dr. Steve helped me a lot during my master's study. Every time the Chinese New Year comes, Professor Steve will give Chinese students a holiday.

I also want to thank Dr. Haitham Khallaf and Mr. Abdallah S. Ghazy. They provided a lot of advice and guidance on my graduation thesis. Mr. Abdallah is like a big brother to me. He is a professional teacher in underwater optical wireless communication study, and I learnt a lot from his research.

In addition, I also want to thank my girlfriend Xiaoxue Kong, who gives me a lot of support and encouragement.

Finally, I want to thank my family for their love.

Contents

List of Figures

List of Tables

Chapter 1

Introduction

According to a recent survey by Nasir Saeed *et al* [1], the status of Underwater Wireless Optical Communications (UWOC), Networks, and Localization are described. According to [6], nearly 97% of the water surface of the earth are oceans. There is a growing interest in ocean exploration and development. Therefore, the research about the underwater sensors and Autonomous Underwater Vehicles (AUV) is growing. Moreover, some AUVs, e.g. OpenROV and the SubSea Glider, require enough understanding of the location information [7]. As a result, research on underwater localization algorithms is becoming essential. This chapter reviews acoustic, radio and optical approaches considered for underwater localization.

1.1 Underwater Wireless Communications

Underwater Wireless Communication (UWC) technology promotes the development and application of underwater exploration. Acoustic waves, radio frequency

and optical waves are the main frequency bands used in underwater communications. Underwater Wireless Optical Communications (UWOC) has the advantages of high bandwidth and high speed compared with traditional radio frequency (RF) and Underwater acoustic wireless communications (UAWC), making it an attractive and feasible alternative. This section compared the UWOC with RF and acoustic methods in more detail, giving the advantages and disadvantages of UWOC.

Acoustic Waves

Underwater acoustic wireless communications can provide communication over relatively long distances since the 1800s. Because of the high demand for military requirements during the World Wars, underwater acoustic communication system has become a well-developed technology and has been used in almost every field of Underwater Wireless Senor Networks (UWSNs) [8]. In 1995, the author in [9] proposed a UAWC system with a data rate of 40 kbps over one nautical mile. In 1996, a UAWC system with a data rate of 8 kbps was developed, which can work at a depth of 20 m and a horizontal distance of 13 km [10]. In 2005, a high-speed UAWC system was designed in [11] which supports a data rate of 125 kbps. In addition, a data rate of 60 kbps UAWC system was illustrated in [12], which can be deployed at a depth of 100 m with a horizontal communication range of 3 km.

Although acoustic methods are the most popular way to enable underwater communications, it also has many technical limitations. At first, according to [13] the typical frequencies used in underwater acoustics are between 10 Hz and 1 MHz, resulting in a relatively low communication data rate of the acoustic channel

(theoretically on the order of kbps). Table 1.1 lists a survey of several commercial acoustic modems. Secondly, because the sound wave has a lower propagation speed than optical wave and radio frequency (approximately 1500m/s for 20 Celsius pure water), the acoustic channel suffers from significant transmission time delay (basically in seconds). Thus it is not possible to use acoustic waves in applications that need real-time data interaction. Thirdly, acoustic transmitters and receivers are usually expensive. For example, the price of an acoustic modem with rugged pressure housing is approximate 3000USD$ [14], and the underwater sensors are usually more expensive than the modem. In addition, acoustic waves used by communication systems and high-power sound navigation and ranging (SONAR) devices can have a harmful impact on the underwater marine wildlife [15].

Acoustic device	Bandwidth	Data rate	Distance
DSPComm AquaComm Mako [16]	14 kHZ	240 bps	100 m
TriTech MicronModem [17]	4 kHz	40 bps	500 m
LinkQuestUWM10000 [18]	5 kHZ	5000 bps	1 km
EvoLogics S2CR7/17 USBL [19]	10 kHZ	6900 bps	8 km
Teledyne BenthosAtm88x [20]	5 kHZ	2400 bps	6 km

TABLE 1.1: Comparison of commercial underwater acoustic devices.

Radio Frequency Waves

RF communication refers to the use of electromagnetic radiation for transferring information between two devices that have no direct electrical connection. Both acoustic and optical waves cannot support smooth transmission through the air/water interface. In contrast, RF waves can cross water-to-air boundaries easily [21]. Moreover, the RF signal is less affected by water turbulence and turbidity effects compared to the optical wave. When compared with acoustic waves, RF

waves have a higher propagation speed and smaller time delay correspondingly [22]. The authors in [23] have improved the capacity of underwater RF systems up to 10 Mbps over a communication distance of 100 m with the frequency of 1 MHz.

However, the data rates of underwater RF communication systems are frequency-dependent and due to the fact that the attenuation of RF waves increases significantly while frequency increases [24]. According to [22] the attenuation of signal is usually between 60dB and 80dB. RF waves are commonly used in shallow water [25]. For instance, submarines can communicate at only up to a depth of 8-10 meters, using very low frequency (VLF) to transmit signals [26] at low data rates of 50 bit/s [27].

Optical Waves

Seawater has a low loss transmission window in the 450nm-550nm wavelength corresponding to the blue-green spectrum shown in the Figure 1.1 [28]. In 1966, Gilbert *et al* confirmed the existence of blue and green light transmission "window" in the water. This "window" provides the possibility for the development of UWOC in the future [29]. In 1977, the researchers from the University of California conceived a unidirectional optical communication system from the coast to the submarine, using a blue-green laser source as the transmitter to generate one-microsecond duration light pulses. The transmitter was designed to be portable, which could be carried by a land vehicle or an aircraft. The transmitter aimed its pulsed beam at a relay satellite in space, then reflected the beam to a submarine's location in a distant ocean. According to the summary in [30], the submarine could receive laser signals at a depth of about 700 m in deep-ocean water on a clear day
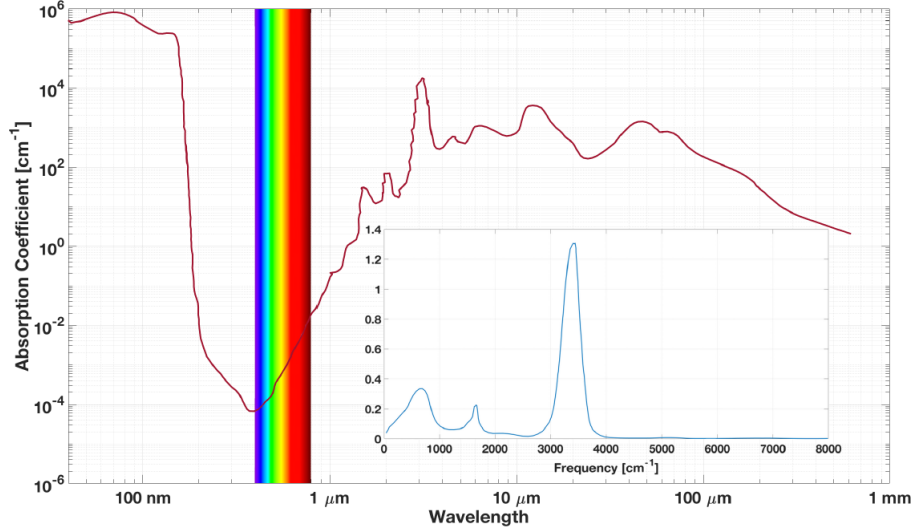
FIGURE 1.1: Attenuation of optical waves in water (figure taken from [1])

or night, and about 570 m on a cloudy day [30]. The US navy held ADORE experiment in 1992, where two-way laser communication between airplane and submarine in the 455 nm bandwidth was demonstrated [31].

For decades, UWOC has remained limited to military applications [30,31]. However, at the beginning of the 20*th* century, some limited UWOC products were commercialized. For example, the BlueComm UWOC system can achieve 10Mbps underwater data transmission over a distance of 150m by using time division multiple access (TDMA) methods, which provides a bi-directional high-speed, low latency link [32]. The Ambalux UWOC system can reach 10Mbps data transmission rate within 40 meters [33]. Compared with radio frequency systems, UOWC can support a higher data transmission rate within 100 meters over several Gbps in clear water with nearly no scattering. In addition, since the light wave speed of the UOWC system can reach $2.25 \times 10^8 m/s$, technically, the system delay is

much lower than those acoustic methods [34, 35]. Table 1.2 lists some experiments of UWOC.

UWOC Ref.	Source	Data rate	Distance
UOWC with vector radiative transfer theory [36]	1 W Laser (532 nm)	1 Gbps	30 - 50 m
UOWC for autonomous robots [37]	500 mW Blue LED (470 nm)	$\approx$ kbps	20-30 m
UOWC with bandwidth dispersion [38]	3 W Laser (532 nm)	5 Gbps	64 m (clear ocean)
UOWC for remote robots [39]	5W LED (480 nm)	1.2 Mbps	200 m
UOWC for sensor networks [40]	0.1 W LED (532 nm)	1 Gbps	31 m (deep ocean)

TABLE 1.2: Summary of UWOC

However, underwater optical communications also have many limitations. The optical beam suffers from absorption, scattering, turbulence, and multi-path fading in the underwater environment [29, 41]. Those phenomena can cause performance degradation and significantly reduce the communication range. The physical origins of those impairments and underwater optical characteristics are introduced in Chapter 2.

1.2 Underwater Optical wireless Localization

Underwater positioning technology is especially important today because underwater optical wireless networks are inseparable from accurate location information [42]. Range based approaches to localization are typically used and consist of two stages:

Stage 1 is the range measurement stage. In Figure 1.2 each target node estimates its distance from each reference node (buoy). In the literature, the received signal strength (RSS) method and time of arrival (TOA) method are the main localization scheme used for UOWNs [42]. Therefore, RSS and TOA methods of ranging are introduced below, and a table of different optical wireless localization
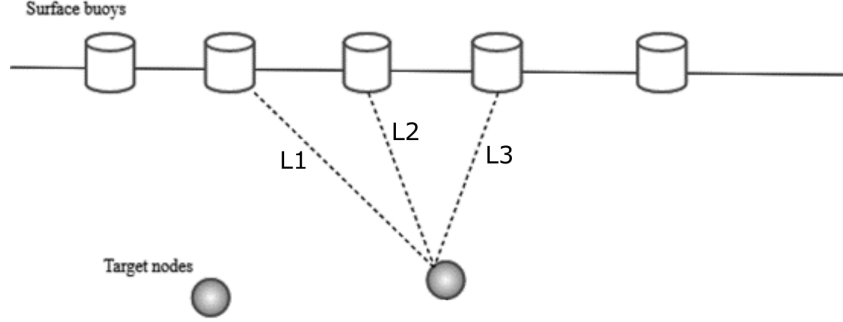
FIGURE 1.2: Stage 1: range measurement

scheme are listed in Table 1.3. The error tolerance depends on applications. For high-speed systems, latency is a key limitation.

Received Signal Strength (RSS): In the RSS method, the distance between the target and neighbouring buoys is estimated based on a known attenuation model. The underwater target needs to compare the received signals from at least four neighbouring buoys to estimate its location. Since almost all receivers have the ability to estimate the strength of the received signal, the RSS method does not need additional devices or modules, which makes it a low-cost method [43]. However, an accurate channel model is essential for distance estimation. For instance, in [43], the author used the following equation as the channel model to describe the relationship between received signal strength $y(i)$ and distance d_i. The channel is assumed to be invariant with time:

$$y(i) = RP_{t,avg}T_s\beta(d_i)L(d_i) + v \tag{1.1}$$

7

Where $R = \eta q/hf$ is represented as the sensor's responsiveness. Denote $P_{t,avg}$ and T_s as the average transmitted power and time duration of the signal from anchored nodes, respectively. And $\beta(d_i)$ is log-normal fading coefficient and $L(d_i)$ is the channel loss caused by absorption and scattering effects (introduced in Section 2.2). The zero-mean Gaussian channel noise is added as v. The RSS method is based on the given signal attenuation model, which means the pairs of $(y(i), d(i))$ from Monte Carlo simulation or experiments should be known in advance. Then the estimation of distance $d(i)$ can be obtained in terms of received signal strength $y(i)$.

Time of Arrival (TOA): The TOA method estimates distances based on the transmission time and underwater light speed [44]. However, the TOA method has a high requirement of time synchronization among all the nodes in the network, including buoys and the target. For example, in [43], the author assumed all the anchored nodes send their optical signals at $t_0 = 0$. The underwater target calculates the TOA of every received signal from the neighbouring anchored nodes, namely t_1, t_2, t_3, and so on. In general, the target needs to know the anchored nodes' clock phase (t_0) to calculate the transmission times. With known t_i and t_0, the target can estimate its distance from the $i-$th anchored node using the following equation

$$\hat{d}_i = \frac{c}{n} t_i$$

where c and n are represented as the speed of light in the vacuum and the refractive index of the water type.

Stage 2 is the location estimation stage. The target node identifies its location

Scheme	Method	Accuracy
Underwater optical CDMA networks [43]	TOA, Optical	MSE=0.25 m (clear seawater)
Underwater optical CDMA networks [43]	RSS, Optical	MSE=1.80 m (clear seawater)
UOWNs localization with limited connectivity [45]	RSS, Opticall	RMSPE=0.1-0.35 m
UOWNs localization with low rank matrix [46]	RSS, Optical	RMSE=0.64 m
UOWNs localization with outlier detection [47]	RSS, Optical	RMSE=0.659 m
UOWNs localization with energy harvesting [48]	RSS, Optical	RMSPE=0.22 m
Hybrid energy harvesting localization system [42]	RSS, Hybrid acoustic/optical	MSE=0.05-1.77 m

TABLE 1.3: Different underwater optical wireless localization schemes (MSE: Mean square error. RMSPE: Root mean square positioning error. RMSE: Root mean square error.)

via the intersection of at least three circles centred at each buoy node with a radius corresponding to the estimated distances, as shown in Figure 1.3. Note that N_1, N_2 and N_3 are reference nodes with known location, and r_1, r_2 and r_3 are measured distances between target and reference nodes (buoys) correspondingly, while E_v is the estimated location. Normally, to estimate the position of a target in n-dimensional space, the number of independently estimated distances should be at least $n + 1$. For example, two measurements in two-dimension space only produce two circles, like the blue and the green circles in Figure 1.3. These circles have two intersection points; unless another measurement is performed, the estimated position cannot be determined. In the three-dimensional space, four measurements from 4 buoys are required, as shown in Figure 1.4, three measurements produce three spheres, and they have two intersection points as well, represented by black dots, which can not be determined as the estimated position. This thesis introduces some typical localization algorithms, including the 3D least square method (LS), 2D particle swarm optimization method (PSO) and 2D majorization-minimization approach (M-M) in Chapter 3. Their comparison of results are discussed in Chapter 4.
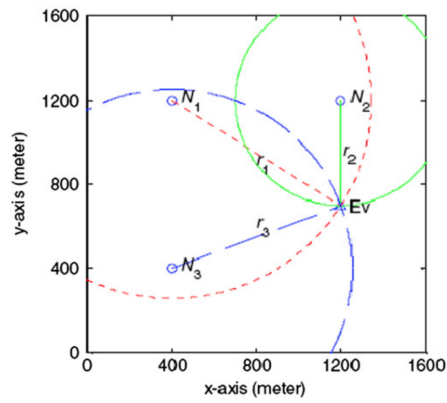
FIGURE 1.3: Illustration of location estimation using circles in 2D space [2]
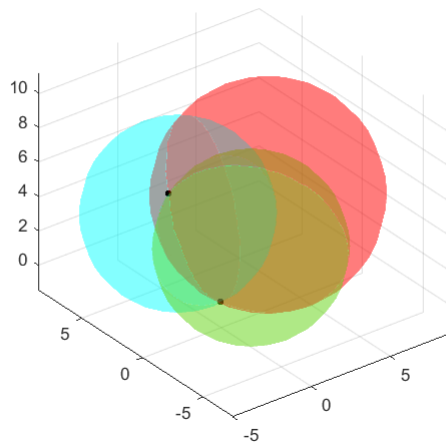
FIGURE 1.4: Illustration of location estimation using spheres in 3D space, produced by Matlab

1.3 Thesis Contributions

In the literature, most underwater targets in the localization or tracking experiments are stationary or with speeds lower than 10m/s. As an example, the author in [49] has developed a low-cost and high-speed AUV for the optical survey of the seafloor. "Hattori," has a maximum surge speed is $2m/s$. In [50] a high-speed AUV-based silent localization system has been proposed; the maximum speed of underwater sensor node is $2m/s$. An underwater optical localization experiment was introduced in [51], Autonomous Modular Optical Underwater Robot (AMOUR) is an AUV developed by MIT with a maximum speed of $1m/s$. However, due to the existence of supercavitating AUVs, the frictional drag of vehicles is reduced dramatically, enabling the underwater vehicle to achieve high speeds of more than $100m/s$ [52] [53].

Hence, this thesis combines existing underwater positioning technology with knowledge of the LED Lambertian pattern to localize underwater. A key contribution of this work is an adaptive time slot approach that helps locate the high-speed underwater target. The signal transmission time of the buoy is regarded as a time slot; where all the buoys continuously transmit signals one after another, these time slots form a time sequence at the transmitter side. However, because the buoys are randomly distributed, the distance from the buoy to the target is not equal. In other words, the underwater propagation time of each buoy is not equal, which leads to discontinuity, overlap, loss of time slots at the receiver side. The adaptive time slot is a secondary distance optimization based on the position and distance information derived from the initial signal. The concept reduces the interference of light signals between multiple buoys and improves positioning

accuracy. The adaptive time slot approach can finish the localization process in micro-seconds. Therefore it can also be used in the sea area where the underwater channel changes quickly. The thesis also studies a 9-buoy distribution scheme, and buoys are deployed at fixed positions, where the RMSE of every point on the $X - Y$ plane at different depths are discussed.

1.4   Thesis Structure

This thesis consists of five chapters. A summary of each chapter is presented as follows:

Chapter 1 introduces the underwater background knowledge and some new applications of UWOC, UAWC and underwater RF communication. Also, the advantages and disadvantages of using UWOC are studied. Advantages include high data transmission rate, low transmission latency and low cost, and disadvantages contain high absorption and scattering, moderate channel range.

Chapter 2 illustrates the underwater optical channel properties and illustrates the system model. A fast localization concept with an adaptive time slot is introduced, designed to improve the positioning reliability. This chapter also introduces several ocean wave models that are widely used at this stage. The Pierson-Moskowitz Spectrum (P-M) method is selected based on oceanographic observations to model the 3D ocean surface.

Chapter 3 introduces 2D underwater localization algorithms, including Particle swarm optimization and Majorization-minimization, and one 3D localization algorithm Least square method. In addition, the concept of the adaptive time slot is

explained in the rest of the chapter.

In Chapter 4, two scenarios and their RMSE results are discussed. The first scenario is the randomly deployed buoys and target; the RMSE results between before and after using the adaptive time slot (ATS) algorithm are compared in Section 4.1. In the second scenario, a practical situation to localize an underwater target with buoys is proposed as the 9-buoy distribution formation, assuming that nine buoys are anchored at the given positions of the simulation surface. Two cases are introduced in Section 4.2. The first case is the 9-buoy distribution scheme with a randomly deployed target, which localization accuracy can be compared with the first scenario in Section 4.1. In contrast, the second case is the target deployed at a given position with various depths; in this case, RMSE error distribution is discussed in Subsection 4.2.2. Majorization-Minimization approach, Particle Swarm Optimization algorithm and the 3D Least Square method are used and compared in both scenarios. In general, the M-M approach gave the best results, whereas, as the depth decreases, the interference from other buoys' optical signals increases, resulting in a decrease in the positioning accuracy of the algorithm.

Chapter 5 summarizes the entire thesis and suggests directions for future work.

Chapter 2

System and Channel Models

In this chapter, some ocean surface models are introduced at first, and then underwater optical wireless channel and system model are discussed.

2.1   3D Ocean Surface Modeling

The simulation of ocean waves can be roughly divided into two methods. The first is based on physics, by solving the Navier-Stokes equation (N-S) of the fluid [54]. The motion state of each particle inside the wave is calculated, thereby simulating ocean waves. However, the process of this equation is very complicated. It is challenging to meet real-time requirements, so the N-S equation is usually simplified to find an approximate solution. For example, Kass [55] simulates water wave animation by simplifying the shallow water equation, Chen [56] uses a numerical iterative method to solve the two-dimensional Navier-Stokes equation. The second approach is based on oceanography. For example, the Pierson-Moskowitz Spectrum (P-M) method [3], which calculates the sea height field through parametric surface synthesis to simulate waves. The following subsections introduce the P-M

spectrum method, including frequency spectrum, direction spectrum, and wave height field, in the end, modelling the ocean surface.

2.1.1 Wave frequency spectrum

Ocean waves are a complicated random process. Pierson first applied Rice's theory of radio noise to ocean waves in the early 1950s [57]. Since then, the use of power spectra to describe ocean waves as a random process has become the main research approach.

Consider superimposing an infinite number of random cosine waves to describe a fixed-point wave surface, denote $Z(t)$ as the wave function with units in meter:

$$Z(t) = \sum_{n=1}^{\infty} a_n \cos\left(\omega_n t + \varepsilon_n\right) \tag{2.1}$$

where a_n and w_n are the amplitude and circular frequency of the component wave respectively, ε_n is the random initial phase uniformly distributed in the range of $0 \sim 2\pi$ and t is time. As shown in Figure 2.1, the thick black line is the result of the superposition of the thin black line and the dashed cosine wave.
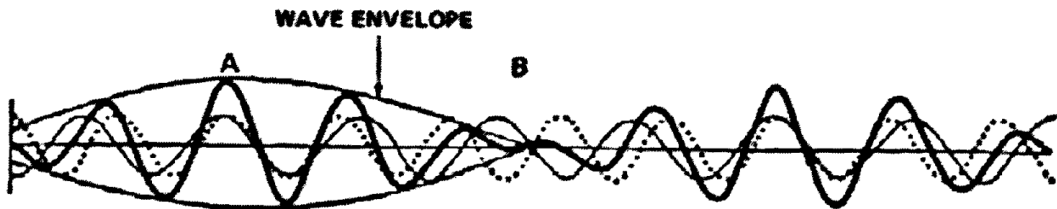
FIGURE 2.1: Wave groups are formed by interference between two or more wave trains of different periods moving in the same direction. [3]

the variance of the sea wave surface in equation 2.1, due to $D[Z] = E[Z^2(t)]$ is:

$$D[Z] \;=\; \sum_{n=1}^{\infty} \int_{0}^{2\pi} a_n^2 \cos^2\left(\omega_n t + \varepsilon_n\right) \frac{1}{2\pi} d\varepsilon \;=\; \frac{1}{2} \sum_{n=1}^{\infty} a_n^2 \qquad (2.2)$$

Define the frequency spectrum as $S(\omega)$, then the variance:

$$D[Z] \;=\; \int_{0}^{\infty} S(\omega) d\omega \qquad (2.3)$$

so,

$$\frac{1}{2} \sum_{n=1}^{\infty} a_n^2 \;=\; \int_{0}^{\infty} S(\omega) d\omega \qquad (2.4)$$

On the other hand, according to wave theory, the energy of the n-th component wave is $\frac{1}{2} a_n^2$. Distribute ω evenly to n constituent waves. The sum energy of the n-th component wave with the frequency in the range of $\omega \sim \omega + \Delta\omega$ is:

$$\sum_{\omega_n}^{\omega_n + \Delta\omega} \frac{1}{2} a_n^2 \;=\; S(\omega_n) \Delta\omega \qquad (2.5)$$

$$S(\omega_n) \;=\; \frac{1}{\Delta\omega} \sum_{\omega_n}^{\omega_n + \Delta\omega} \frac{1}{2} a_n^2 \qquad (2.6)$$

Therefore, $S(\omega_n)$ represents the average power within a frequency interval of $\Delta\omega$. Each component wave provides the total power of the ocean wave, and the

function $S(\omega_n)$ gives the power provided by the component waves in different frequency intervals, so $S(\omega_n)$ represents the distribution of ocean wave power relative to the frequency of each component waves. If $\Delta\omega = 1$, Equation (2.6) represents the power within the unit frequency interval, that is the power density, so $S(\omega_n)$ is called the *power spectrum*. Because it gives the distribution of power relative to frequency, it is also called frequency spectrum. Figure 2.2 is a diagram of wave spectrum, where $f = \frac{\omega}{2\pi}$.
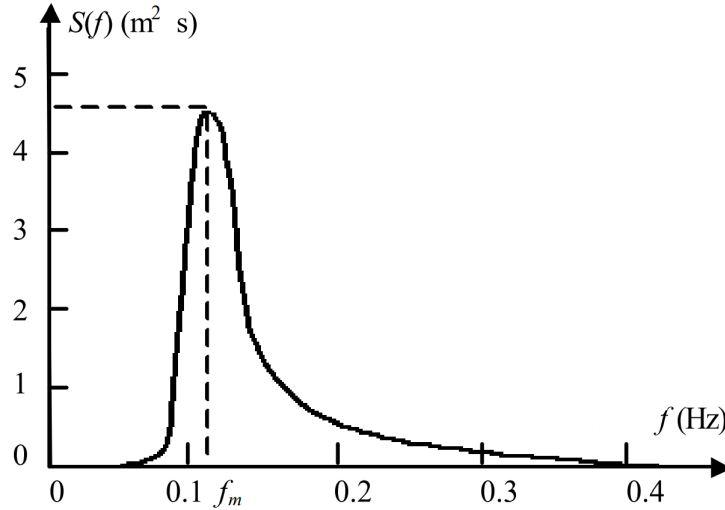
FIGURE 2.2: Wave spectrogram [4]

At present, the most common wave spectrums include the Bretschneider spectrum and Pierson-Moscowitz (P-M) spectrum, JONSWAP spectrum, and Phillips spectrum [3].

The Bretschneider spectrum (developed in 1956 [58]) comes from observations in the deep waters of the North Atlantic without wind or large waves. This work was improved to the P-M spectrum (in 1964, Pierson-Moscowitz spectrum, [59]), which assumes that the wave satisfies the Gaussian stochastic process and is a fully

grown wave. In contrast, the JONSWAP spectrum (The Joint North Sea Wave Observation Project in 1973, [60]) is assumed the wave to be never fully grown. While the Phillips (in 1957, [61]) spectrum is a statistical model in which wind speed is regarded as the random contribution of pressure changes [3] and is mainly used to describe the dynamic effect of wind blowing on the water surface. However, the P-M spectrum is used as the basis for standardization of the prediction of marine vessels and offshore structures in the open ocean [3]. Therefore, this thesis uses the P-M spectrum as the modelling method. Its expression is [3]:

$$S(\omega_n) \;=\; \frac{\alpha g^2}{\omega_n^5} \exp\left[-\beta\left(\frac{g}{U\omega_n}\right)^4\right] \tag{2.7}$$

where $\alpha = 8.1 \times 10^{-3}$, $\beta = 0.74$, $\alpha g^2 = 0.78$, g denotes the acceleration of gravity and U is the wind velocity at a height of 19.5m above the ocean surface. Taking the partial derivative of the frequency ω and set the partial derivative to zero to obtain the spectrum peak frequency ω_m:

$$\frac{\partial S(\omega)}{\partial \omega} \;=\; \frac{\alpha g^2}{\omega^6}\left(-5 + 4\beta\left(\frac{g}{U\omega}\right)^4\right)\exp\left[-\beta\left(\frac{g}{U\omega}\right)^4\right] \;=\; 0 \tag{2.8}$$

$$\omega_m = \frac{(0.8\beta)^{\frac{1}{4}}g}{U} \;=\; \frac{8.596}{U} \tag{2.9}$$

2.1.2 Wave direction spectrum

Equation 2.1 describes only the change of the wave surface at a fixed point over
time. The actual ocean surface is three-dimensional, and its energy is not only
distributed in a certain frequency range but also a fairly wide range of directions.
Equation 2.1 can be expanded by considering the superposition of most cosine
waves with amplitude a_n, frequency ω_n, initial phase ε_n, and propagating in the x
and y horizontal planes along the θ_n angle with respect to the x axis. Therefore,
the wave function $Z(t)$ becomes $Z(x, y, t)$ with changing position (x, y) and time t.
As shown in the following formula (k_n is the wave number of the $n-th$ component
wave, $-\pi \leq \theta_n \leq \pi$):

$$Z(x, y, t) = \sum_{n=1}^{\infty} a_n \cos\left[k_n(x cos\theta_n + y sin\theta_n) - \omega_n t + \varepsilon_n\right] \qquad (2.10)$$

As for the deep water situation, according to the linear wave theory [4] :

$$\omega_n^2 = k_n g \qquad (2.11)$$

where d is the depth of the water. Substituting the above formula into Equation
(2.10):

$$Z(x, y, t) = \sum_{n=1}^{\infty} a_n \cos\left[\frac{\omega_n^2}{g}(x \cos \theta_n + y \sin \theta_n) - \omega_n t + \varepsilon_n\right] \qquad (2.12)$$

The above formula shows that the wavefront at any time t has various directional
angles of $\theta_n(-\pi \leq \theta_n \leq \pi)$ with respect to $x - axis$ and various frequencies
$\omega_n(0 \leq \omega_n \leq \infty)$, which consists of infinite composition waves. Assuming phase

factor ε_n is a uniformly distributed random variable in the range of $0 \sim 2\pi$ and $a_n \geq 0$. For any component wave within a frequency interval $\Delta\omega$ and a direction interval $\Delta\theta$, its energy is $\frac{1}{2}a_n^2$. Similar to the frequency spectrum in the previous Section 2.1.1, the directional spectral density function $S(\omega_n, \theta_n)$ can be obtained as:

$$\sum_{\Delta\theta}\sum_{\Delta\omega}\frac{1}{2}a_n^2 = S(\omega_n, \theta_n)d\omega d\theta \tag{2.13}$$

$$0 \leq \omega_n < \infty, \quad -\pi \leq \theta_n \leq \pi \tag{2.14}$$

The direction spectrum $S(\omega_n, \theta_n)$ gives the distribution of the power of each component wave in different directions with respect to the frequency, in other words, for a given frequency, $S(\omega_n, \theta_n)$ shows the division of the power of each component wave with respect to the direction, in theory, the range of θ varies from $-\pi \sim \pi$, whereas, the wave energy is mostly distributed within the range of $\frac{\pi}{2}$ [4].

The following relationship exists between the direction spectrum and power spectrum of ocean waves at the same location:

$$S(\omega) = \int_{-\frac{\pi}{2}}^{\frac{\pi}{2}} S(\omega, \theta)d\theta \tag{2.15}$$

with wave surface variance:

$$D[Z] = \sigma^2 = \int_{-\frac{\pi}{2}}^{\frac{\pi}{2}} \int_0^\infty S(\omega, \theta) d\omega d\theta \tag{2.16}$$

Normally, the direction spectrum $S(\omega, \theta)$ can be written as the product of the frequency spectrum and the direction function [4]:

$$S(\omega, \theta) = S(\omega)G(\omega, \theta) \tag{2.17}$$

where $S(\omega)$is the frequency spectrum, and $G(\omega, \theta)$ is the direction distribution function, referred to as the direction function. The direction function used in this thesis when simulating ocean waves is based on the formula obtained from the Wave Stereo Observation Project (referred to as SWOP-Stereo Wave Observation Project) [62]:

$$G(\omega_n, \theta_n) = \frac{1}{\pi}(1 + p\cos 2\theta + q\cos 4\theta), \quad |\theta| \leq \frac{\pi}{2} \tag{2.18}$$

empirical factors defined as:

$$p = (0.5 + 0.82\exp[-\frac{1}{2}(\frac{\omega_n}{\omega_m})^4]) \ , \quad q = 0.32\exp[-\frac{1}{2}(\frac{\omega_n}{\omega_m})^4] \tag{2.19}$$

2.1.3 Wave modelling

After introducing the height field, frequency spectrum and direction spectrum in detail, 3D sea surface can be concluded in Figure 2.3. According to Equation (2.12), when implemented, the number of waves forming the wave height field cannot be infinity, and there can only be a finite number of k. Suppose the number of frequency dispersion is N and the number of direction angle dispersion is M, and define $K = N \times M$. Since the frequency of the component waves forming the ocean wave is mainly concentrated in a lower frequency band, this range is (ω_1, ω_N) selected from [59], and the frequency component waves outside this range contribute little to the energy of the ocean wave. Dividing the frequency in $S(\omega_1, \omega_N)$, into N segments according to the frequency equal division method, each interval is $\Delta\omega$, where $\Delta\omega = (\omega_N - \omega_1)/N$. In the interval (ω_1, ω_N), taking ω_i or ω_N as the discrete points in the interval to find the corresponding frequency spectrum $S(\omega_i)$, or other values. The discrete point value taken in this thesis is the frequency mean value poison in the interval $\frac{1}{2}(\omega_1, \omega_N)$, and its corresponding frequency spectrum is $S(\frac{1}{2}(\omega_1, \omega_N))$. In simulation, $N = 10, M = 8$. Note that larger N and M give more details about the sea surface.

In the same way, the direction angle θ can also be equally divided into M sections, each interval is $\Delta\theta$, where $\Delta\theta = (\theta_M - \theta_1)/M$. The calculation formula for the wave height field after the frequency and direction angle becomes:

$$Z(x, y, t) = \sum_{i=1}^{N} \sum_{i=1}^{M} a_{i,j} \cos[\frac{w_i^2}{g}(x\cos\theta_j + z\sin\theta_j) - w_i t + \varepsilon_i] \qquad (2.20)$$

where, as shown in Figure 2.4, $Z(x, z, t)$ represents the instantaneous height of
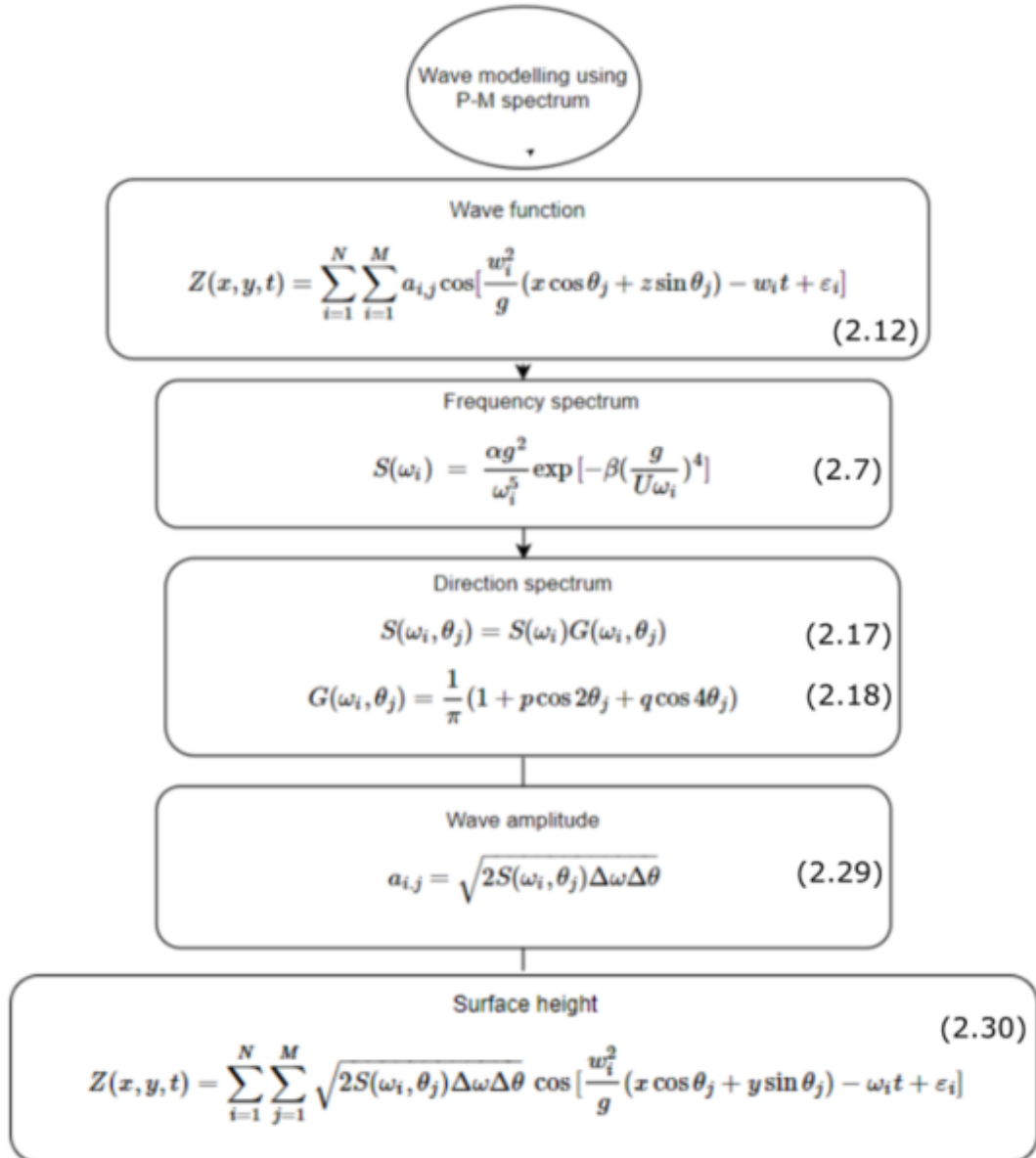
FIGURE 2.3: Block diagram of modelling P-M spectrum ocean surface
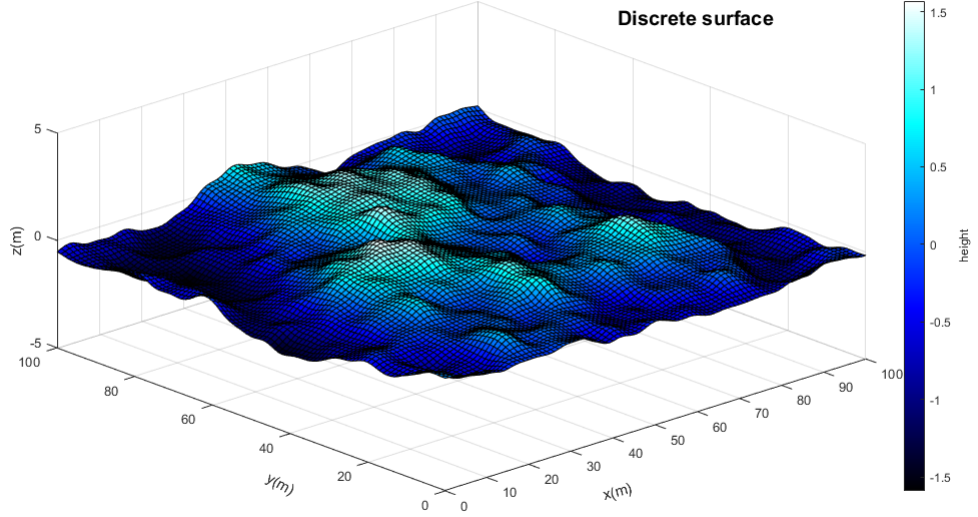
FIGURE 2.4: Height field at sampled points with 1 meter interval

the grid sampling point on the sea level $X - Y$ plane at time t, and $a_{i,j}$ represents the component wave amplitude with a frequency of ω_i and a direction angle of θ_j. The only unknown parameter is the amplitude $a_{i,j}$, which is described in Equation 2.27. The frequency spectrum and direction spectrum of the P-M spectrum are shown in Equation 2.7 and Equation 2.17.

$$S(\omega_i) \;=\; \frac{\alpha g^2}{\omega_i^5} \exp\left[-\beta(\frac{g}{U\omega_i})^4\right] \tag{2.21}$$

$$S(\omega_i, \theta_j) = S(\omega_i)G(\omega_i, \theta_j) \tag{2.22}$$

24

where n is replaced by i and j, represented as the i-th frequency component and j-th direction component respectively. Correspondingly:

$$G(\omega_i, \theta_j) = \frac{1}{\pi}(1 + p\cos 2\theta_j + q\cos 4\theta_j) \tag{2.23}$$

$$p = (0.5 + 0.82\exp[-\frac{1}{2}(\frac{\omega_i}{\omega_m})^4]) \;, \quad q = 0.32\exp[-\frac{1}{2}(\frac{\omega_i}{\omega_m})^4] \;, \quad |\theta| \leq \frac{\pi}{2} \tag{2.24}$$

where the spectrum peak frequency ω_m is given by Equation 2.8 and Equation 2.9.

Substituting Equation (2.24) into Equation (2.23), $G(\omega_i, \theta_j)$ can be found, which frequency is ω_i and direction angle is θ_j. Substituting Equation (2.23) and Equation (2.21) into Equation (2.22), $S(\omega_i, \theta_j)$ can be obtained. According to Equation 2.14, the sum of wave power of the direction spectrum is:

$$\sum_{\theta_j}^{\theta_j+\Delta\theta} \sum_{\omega_i}^{\omega_i+\Delta\omega} \frac{1}{2}a_{i,j}^2 \; = \; S(\omega_i, \theta_j)\Delta\omega\Delta\theta \tag{2.25}$$

$$0 \leq \omega < \infty, \quad -\pi \leq \theta \leq \pi \tag{2.26}$$

then, the value of $a_{i,j}$ can be estimated as:

$$a_{i.j} = \sqrt{2S(\omega_i, \theta_j)\Delta\omega\Delta\theta} \tag{2.27}$$

In the end, find the instantaneous height Z of the grid sampling point on the seaplane at (x, y) when time t:

$$Z(x, y, t) = \sum_{i=1}^{N} \sum_{j=1}^{M} \sqrt{2S(\omega_i, \theta_j)\Delta\omega\Delta\theta} \, \cos\left[\frac{w_i^2}{g}(x\cos\theta_j + y\sin\theta_j) - \omega_i t + \varepsilon_i\right]$$

$$(2.28)$$

where the phase factor ε_n is a uniformly distributed random variable in the range of $0 \sim 2\pi$.

2.2 Underwater Optical Channel Characteristics

There are two main groups of the optical properties of water: Inherent optical properties (IOPs) and Apparent optical properties (AOPs).

IOPs depend only on the transmission medium, more specifically, the components of the medium and the types of the particles in it [63]. They do not depend on the characteristics of the light source. It mainly includes absorption coefficient, scattering coefficient, attenuation coefficient and volume scattering function (VSF) [64].

Whereas AOPs depend on the situations of the light field and the transmission medium. Including diffuse attenuation coefficient and collimation coefficient [63].

In underwater environment, according to the Beer-Lambert law, the widely used function to characterize the light attenuation effects in various underwater

situations [65] expressed as:

$$I = I_0 e^{-c(\lambda)L} \tag{2.29}$$

where I is the received light intensity, I_0 is the transmitted light intensity, L is the transmission distance, and $c(\lambda)$ is the attenuation coefficient. The overall attenuation effects can be divided into absorption and scattering, expressed as the Equation 2.30 [66]:

$$c(\lambda) = a(\lambda) + b(\lambda) \tag{2.30}$$

The unit of attenuation coefficient is m^{-1}. Specifically, there are four main factors that compose the overall optical absorption coefficient, represented as [67]:

$$a(\lambda) = a_w(\lambda) + a_{CDOM}(\lambda) + a_{phy}(\lambda) + a_{det}(\lambda) \tag{2.31}$$

where $a_w(\lambda)$ is the absorption of pure seawater, which is mainly caused by water molecules and dissolved salt such as $NaCl$, $MgCl_2$, Na_2SO_4, and KCl [68]. The absorption of CDOM (chromophoric dissolved organic matter) [69] is represented as $a_{CDOM}(\lambda)$, which has high absorption in the blue wavelengths and less absorption in the yellow and red wavelengths [70] [71]. Denote $a_{phy}(\lambda)$ as the absorption of phytoplankton, which is mainly caused by chlorophyll [72]. And $a_{det}(\lambda)$ represents the absorption of detritus. Living organic particles, such as bacteria, zooplankton, detrital organic matter and suspended inorganic particles such as quartz and clay are the sources of $a_{det}(\lambda)$ [73].

The scattering coefficient $b(\lambda)$ can also be affected by those four factors:

$$b(\lambda) = b_w(\lambda) + b_{CDOM}(\lambda) + b_{phy}(\lambda) + b_{det}(\lambda) \tag{2.32}$$

Where $b_w(\lambda)$ is the scattering factor of pure seawater, which is affected by the variations of flow, salinity, and temperature. The scattering factor of CDOM is represented as $b_{CDOM}(\lambda)$. In addition, $b_{phy}(\lambda)$ and $b_{det}(\lambda)$ are the scattering factors due to phytoplankton and detritus respectively, they account for more than 40% of the total scattering effects [74]. Compared with absorption, scattering is relatively independent of wavelength [25].

However, the attenuation coefficient $c(\lambda)$ can be used in the case of a narrow collimated light beam [75]. For instance, when the transmitter is a laser diode, whereas, when a diffuse light source is used at the transmitter side, such as an LED, $c(\lambda)$ does not characterize the light propagation adequately and should be replaced by the so-called diffuse attenuation coefficient that is K_d [76]. The channel loss (Equation 2.30) can be changed to:

$$I = I_0 \exp(-K_d(\lambda)L) \tag{2.33}$$

where K_d is different due to different water type, pure seawater is used in the simulation, hence the $K_d \approx 0.0519 m^{-1}$ at wavelength $\lambda = 530 nm$ [77].

2.3 System and Channel Model

2.3.1 Randomly deployed buoy scenario

In general, two situations are considered. In the first scenario, a fast underwater optical localization situation is assumed, where ten buoys are randomly deployed on the ocean surface. Assuming the buoys are anchored to the seafloor and are not moving. In contrast, their depth and orientation are affected by the surface waves resulting from the wind. One high-speed underwater target is also randomly released in a $100m \times 100m \times 80m$ area. As shown in Figure 2.5, Matlab generates the 3-D ocean surface using the Pierson-Moskowitz Spectrum (P-M) as wave model, as defined in Section 2.1. The average height of the sea surface is 0 meters, which means the surface is moving around at $z = 0m$, and the red dots represent surface buoys, and the red arrows represent their direction vectors. Those buoys' directions are influenced by a sea wave, which includes the attitude angle information. The black cross represents the underwater target, and the green lines are the channel links between buoys and the target.

A general structure is illustrated in Figure 2.6, which shows the corresponding channel link geometry, where the target's receiver R_X is located at depth D and the buoy's transmitter T_X is floating on the surface, where there is a position displacement of R_X with respect to the T_X. In other words, the receiver is, in general, not directly underneath the transmitter. The 3D position of transmitter and receiver are $a_{T_X} = [x_t, y_t, z_t]^T$ and $a_{R_X} = [x_r, y_r, z_r]^T$ respectively. Denote the direction vectors to the T_X and the R_X by $\hat{n}_t$ and $\hat{n}_r$, which include the attitude angle information. $\hat{n_{to}} = [0, 0, -1]^T$ and $\hat{n_{ro}} = [0, 0, 1]^T$ are the original normal
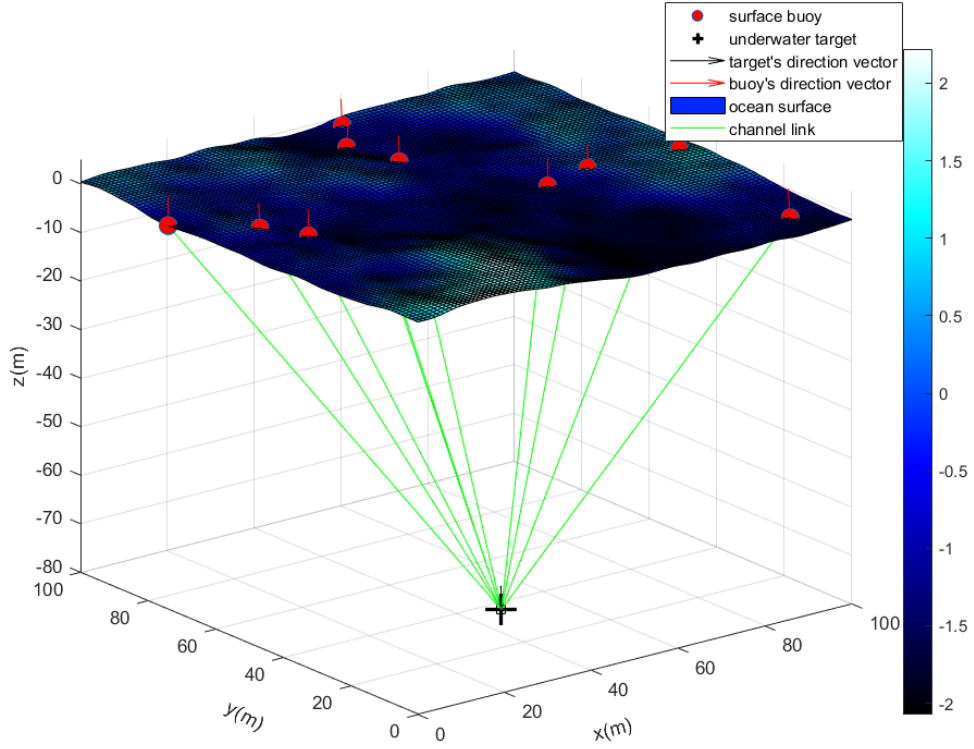
FIGURE 2.5: Randomly deployed buoys and one underwater target.

vectors of the transmitter and receiver without any attitude angle.

At the transmitter side T_X, the surface buoys can receive GPS signals, which implies that they can infer their positions, whereas the underwater target cannot. Every buoy has an LED light source emitting a downwards signal at wavelength 532 nm. The sent signal has a time duration $T = 10\mu s$, which contains buoy's attitude angle information and position information ($[X_t, Y_t, Z_t]$). Those buoys are equipped with gyros, which means they know their attitude angles (including θ_t and φ_t). The LED transmitter under the buoy is assumed following a Lambertian pattern with order m in the following Equation 2.34, which is associated with the
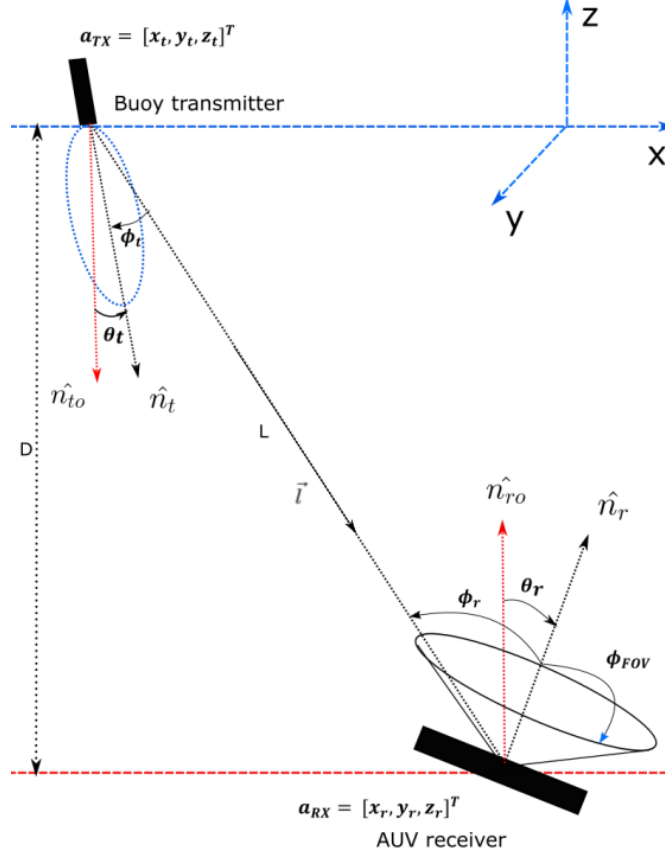
FIGURE 2.6: Transmitter and receiver with position displacement

optical beam directionality [78].

$$P_{R_X} = P_{T_X} \frac{m+1}{2\pi} \ \cos^m(\phi_t) \ e^{-(LK_d)} \ \frac{A_{eff}(\phi_r)}{L^2} \ \prod(\frac{\phi_r}{\phi_{FOV}}) \qquad (2.34)$$

$$m = \frac{-ln(2)}{ln(cos\phi_{1/2})} \qquad (2.35)$$

where m is the Lambertian order and $\phi_{1/2}$ is the half power angle of T_x. The diffuse attenuation coefficient K_d is a measure of how light dissipates with depth in water. In the simulation, the ocean water is pure clear and pure sea water

diffuse attenuation coefficient $K_d = 0.0519$ [77] is used. And A_{PD} is defined in [78] as an active area of the PD, the effective R_X light collection area A_{eff} is then given :

$$A_{eff}(\phi_r) = \begin{cases} A_{PD}\ T_S(\phi_r)\ g(\phi_r)\ \cos(\phi_r), & \phi_r \le \phi_{FOV} \\ \\ 0, & \phi_r > \phi_{FOV} \end{cases} \tag{2.36}$$

where

$$g(\phi_r) = \frac{n_r{}^2}{\sin^2(\phi_{FOV})} \tag{2.37}$$

and ϕ_{FOV} represents the field of view of R_X.

$$\cos(\phi_t) = \frac{\hat{n}_t \cdot (a_{R_X} - a_{T_X})}{||a_{R_X} - a_{T_X}||} \tag{2.38}$$

and

$$\cos(\phi_r) = \frac{\hat{n}_r \cdot (a_{R_X} - a_{T_X})}{||a_{R_X} - a_{T_X}||} \tag{2.39}$$

where $||a_{R_X} - a_{T_X}|| = L$. Denote the position coordinates of the T_X and the R_X by vectors $a_{T_X} = [x_t, y_t, z_t]^T$ and $a_{R_X} = [x_r, y_r, z_r]^T$ respectively.

At the receiver side R_X, a gyro is also assumed to be used on the high-speed underwater target so that it can know its attitude angle underwater. Moreover, it is assumed that the speed of the receiver is $100 m/s$. Its receiver collecting light signals from above, in the front of the photodiode, an optical filter with signal transmission $T_s(\phi_r)$ is used to reject the background noise and mitigate the impact of sunlight as far as possible [79] and no receiver noise is considered in the simulation. The refractive index is n_r and $g(\phi_r)$ is the gain from concentrator, where $\phi_r \in \{0, \frac{\pi}{2}\}$ is the incidence angle [78].
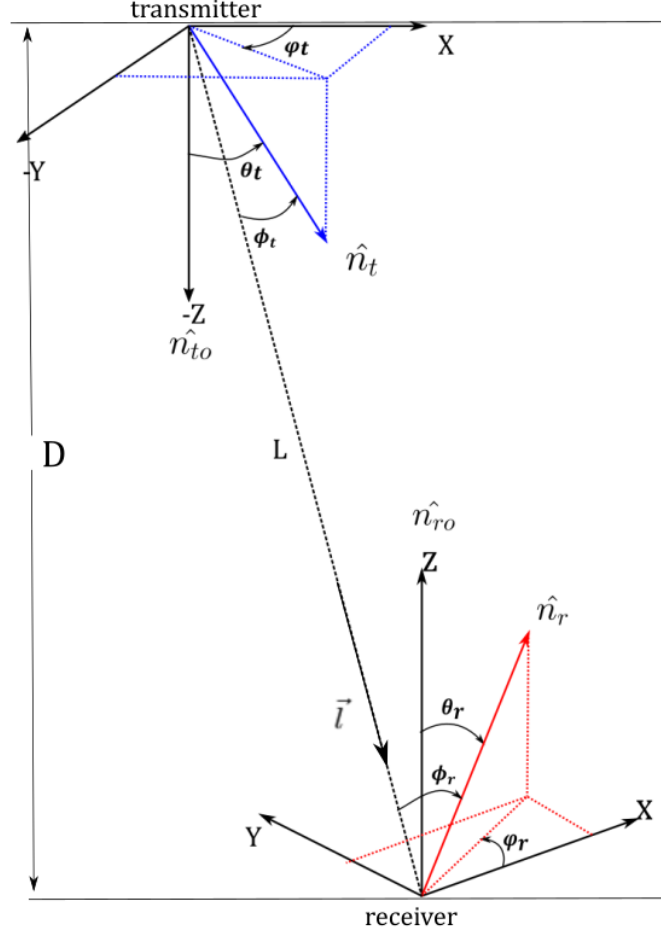
FIGURE 2.7: Link structure between transmitter and receiver

The link structure is shown in Figure 2.7. Assuming the receiver has a light direction sensor, which can detect the direction of incident light as a direction vector $\vec{l}$, and angle ϕ_r can be calculated correspondingly. However, according to [80], a random angle of arrival error with a maximum of 2° degree over FOV is assumed in the simulation. For a given transmitted optical power P_{T_X} and a given received light power P_{R_X}, the LED Lambertian Equation 2.34 can be used to calculate the estimated distance L. The angle of arrival ϕ_r can be obtained by using an on-chip light direction sensor or the AMIMO system proposed in [81].

Combining the incident light direction vector $\vec{l}$ with buoy's transmitter direction vector $\hat{n}_t$, the angle ϕ_t between them can be obtained using Equation 2.40:

$$\cos(\phi_t) = \frac{\vec{l} \cdot \hat{n}_t}{|\vec{l}| \, |\hat{n}_t|} \qquad (2.40)$$

Since the estimated distances from buoys to the underwater target are obtained from stage 1, some localization algorithms can be used to calculate the estimated position of the underwater target, which will be shown in Chapter 3.

Assuming ten buoys continuously sending signals one by one requires a transmission time of $10\mu s \times 10 = 100\mu s$, the underwater target's movement is $100m/s \times 100\mu s = 0.01m$. Thus, it is reasonable to assume a quasi-static assumption that the target is fixed during the localization operation. However, because the buoys are randomly distributed, the distance from the buoy to the target is not equal; in other words, the propagation time of each buoy's signal is not equal, which leads to discontinuity, overlap, loss, of time slots at the receiver side. In Section 3.2, an adaptive time slot approach is introduced as the second estimated distance optimization based on the position and distance information derived from the initial signal. The approach is designed to reduce the interference of light signals between multiple buoys and improve positioning accuracy, which is shown in the section 3.2. Moreover, numerical results comparing before and after using the adaptive time slot are shown in Chapter 4.

2.3.2 Fixed 9-Buoy distribution scheme scenario

In the second scenario, as Figure 2.8 shows, a 9-buoy distribution formation is studied, assuming that buoys are anchored in the given position of the simulation
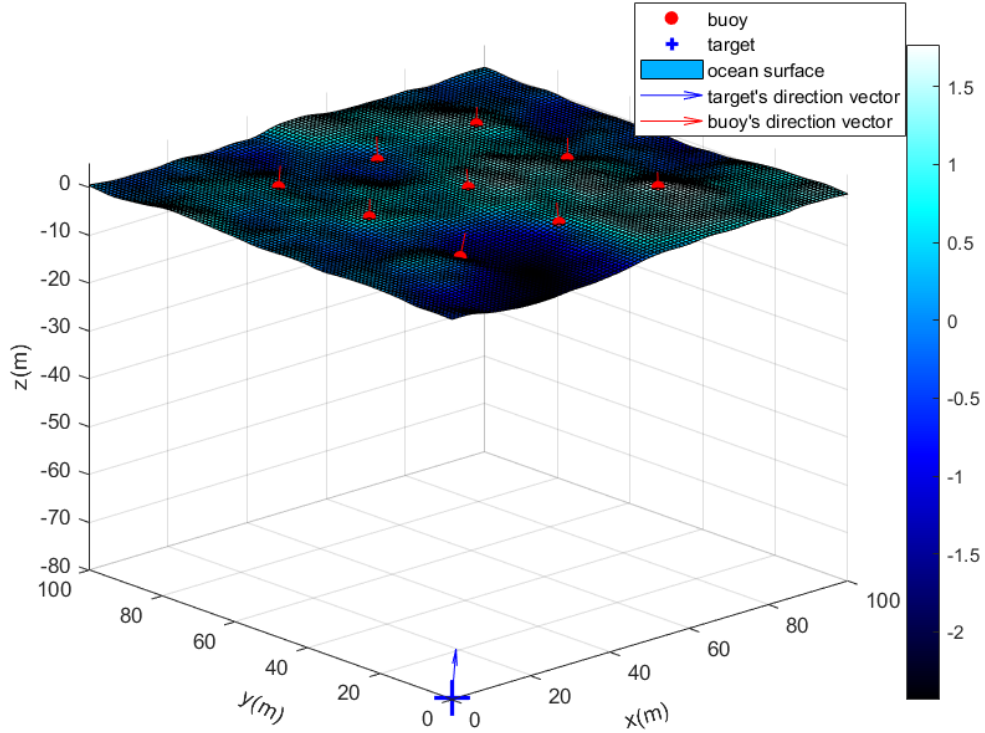
FIGURE 2.8: 9-buoy distribution scheme

area at 25-meter intervals horizontally and vertically, i.e., $x, y \in [25m, 50m, 75m]$. One target can be randomly deployed as the first scenario, and it can also be deployed in a given underwater position. In the simulation, the comparison results of different localization algorithms are discussed, which are shown in Chapter 4.

2.4 Conclusions

In this chapter, firstly, the P-M spectrum method of simulating 3D ocean surface and underwater optical channel properties is introduced. Secondly, the system and channel model are illustrated. Moreover, two situations are considered, the first one is the fast underwater optical localization concept with adaptive time slot

designed to improve the positioning accuracy, buoys and underwater target are randomly deployed, and the second situation is the 9-buoy distribution formation, buoys and target are deployed at given positions, and the RMSE results at different depths using different localization algorithms are discussed in Chapter 4.

Chapter 3

Underwater Localization Algorithms

Chapter 2 introduces the first step of underwater optical wireless localization, the range measurement. This chapter introduces some typical 2D and 3D localization algorithms used in the simulations. The proposed adaptive time slot (ATS) approach for high-speed underwater localization is then illustrated.

3.1 Localization algorithms

The second step of underwater localization is the position estimation, which is carried out using the distance measurements from step one.

3.1.1 3-Dimensional Localization Algorithms

There are many exist range-based location estimation algorithms, such as Analytical method (AM) [82], Least Squares method (LS) [83], Taylor Series method

(TS) [84], Approximate Maximum Likelihood method (AML) [85], and Genetic Algorithm (GA) [86]. In this section, the 3D range-based location estimation algorithm based on least-square method is reviewed.

The position of the target node is determined as the intersection of all the spheres as illustrated in Section 1.2 in Figure 1.4. Notice that the centers of the spheres are the coordinates of the buoys, while the radius is derived from the estimated range of each buoy. Each of the spheres can be described as below:

$$(x_t - x_i)^2 + (y_t - y_i)^2 + (z_t - z_i)^2 = \hat{d_i}^2, \ i = 1, 2, ..., n \qquad (3.1)$$

where $\mathbf{b_i} = (x_i, y_i, z_i)$ and $\hat{d_i}, i = 1, 2, ..., m$ are the known coordinates of the $i-th$ buoy and the estimated range respectively. The index i also indicates the transmitting order in time, for example, the first buoy transmit its signal when $i = 1$. Let m denote the number of buoys in the system. The coordinate of the target to be estimated is denoted as $\mathbf{x} = (x_t, y_t, z_t)$.

Least Squares Method

The most straightforward method for determining the target's coordinate is to find the solution to the nonlinear equation, e.g., least-square method [83]. Subtracting the first buoy's coordinates ($i = 1$) from all other buoys (Equation 3.1) into a form of a matrix, one of the second-order parts $x_t^2 + y_t^2 + z_t^2$ can be cancelled, and the other second-order parts $x_i^2 + y_i^2 + z_i^2$ can be represented as the squared

distances r_i^2 between the i-th buoy and the origin. The matrix should at least has four measurements as mentioned in Section 1.2:

$$2 \begin{bmatrix} x_2 - x_1 & y_2 - y_1 & z_2 - z_1 \\ x_3 - x_1 & y_3 - y_1 & z_3 - z_1 \\ & \dots & \\ x_m - x_1 & y_m - y_1 & z_m - z_1 \end{bmatrix} \begin{bmatrix} x_t \\ y_t \\ z_t \end{bmatrix} = \begin{bmatrix} \hat{d_1}^2 - \hat{d_2}^2 + r_2^2 - r_1^2 \\ \hat{d_1}^2 - \hat{d_3}^2 + r_3^2 - r_1^2 \\ \dots \\ \hat{d_1}^2 - \hat{d_m}^2 + r_m^2 - r_1^2 \end{bmatrix} \tag{3.2}$$

where

$$r_i^2 = x_i^2 + y_i^2 + z_i^2, \quad i = 1, 2, ..., n \tag{3.3}$$

Equation 3.2 can be rewritten as:

$$\mathbf{A}\mathbf{x} = \mathbf{E} \tag{3.4}$$

where $\mathbf{x} = [x_t \ y_t \ z_t]^T$ is the estimated position, and

$$\mathbf{A} = 2 \begin{bmatrix} x_2 - x_1 & y_2 - y_1 & z_2 - z_1 \\ x_3 - x_1 & y_3 - y_1 & z_3 - z_1 \\ & \dots & \\ x_m - x_1 & y_m - y_1 & z_m - z_1 \end{bmatrix}, \quad \mathbf{E} = \begin{bmatrix} \hat{d_1}^2 - \hat{d_2}^2 + r_2^2 - r_1^2 \\ \hat{d_1}^2 - \hat{d_3}^2 + r_3^2 - r_1^2 \\ \dots \\ \hat{d_1}^2 - \hat{d_n}^2 + r_n^2 - r_1^2 \end{bmatrix} \tag{3.5}$$

39

The coordinates of the target will not meet all the equations in the Equation 3.4, so set the error vector as $\mathbf{e} = \mathbf{Ax} - \mathbf{E}$, take the square sum of the error in the error vector, then there is:

$$F(\mathbf{x}) = |\mathbf{e}|^2 = \mathbf{e}^T\mathbf{e} = (\mathbf{Ax} - \mathbf{E})^T(\mathbf{Ax} - \mathbf{E}) \tag{3.6}$$

If the squared error is to be minimized, taking the derivative of the above formula with respect to $\mathbf{x}$, so that the derivative is equal to 0, the expression is:

$$\frac{dF(\mathbf{x})}{d\mathbf{x}} = 2\mathbf{A}^T\mathbf{Ax} - 2\mathbf{A}^T\mathbf{E} = 0 \tag{3.7}$$

where the estimated position $\mathbf{x}$ can be obtained by using following equation [83]:

$$\mathbf{x} = (\mathbf{A}^T\mathbf{A})^{-1}\mathbf{A}^T\mathbf{E} \tag{3.8}$$

3.1.2   2-Dimensional Localization Algorithms

Although the three-dimensional positioning algorithms are the most complete for underwater applications, sometimes the depth information can be obtained with the help of underwater pressure sensors [2], e.g. the pressure sensor, ImpactSubsea ISD4000 has a 0.01% Full-Scale accuracy with the pressure range 10 bar- 600 bar [87]. In this case, the problem can be transformed into a two-dimensional problem. Another method to estimate depth proposed in this thesis is to use an on-chip directional sensor to estimate the angle of arrival, as shown in Figure 3.1.

The directional light sensor can estimate the vector $\vec{l}$, which is the direction vector of estimated distance L. Combine the incident light direction vector $\vec{l}$ with buoy's transmitter direction vector $\hat{n}_t$, the angle ϕ_t between them can be obtained using Equation 3.9:

$$\cos(\phi_t) = \frac{\vec{l} \cdot \hat{n}_t}{|\vec{l}| \, |\hat{n}_t|} \tag{3.9}$$

Substituting arrival angle ϕ_r and transmitted angle ϕ_t into the Lambertian emis-
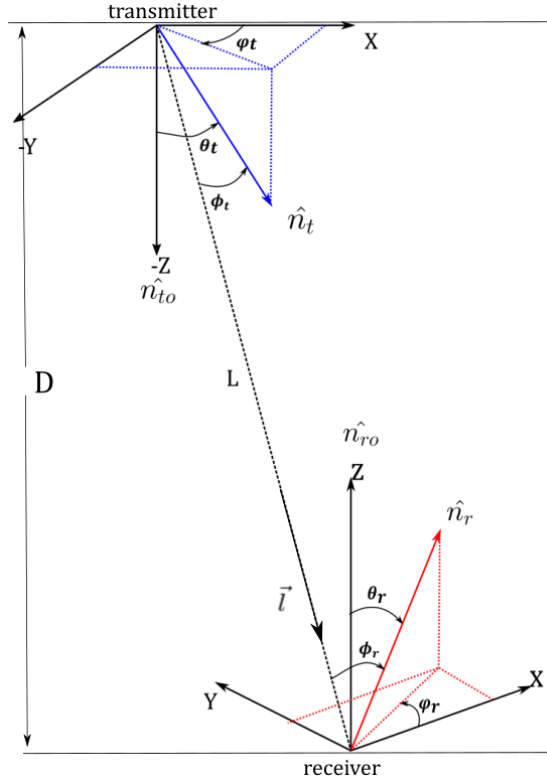
FIGURE 3.1: Orientation of target and Buoy ($\hat{n}_t$ and $\hat{n}_r$ are the direction vectors of transmitter and receiver)

sion pattern:

$$P_{R_X} = P_{T_X} \frac{m+1}{2\pi} \, \cos^m(\phi_t) \, e^{-(LK_d)} \, \frac{A_{eff}(\phi_r)}{L^2} \, \prod(\frac{\phi_r}{\phi_{FOV}})$$

the estimated spatial distance L can be obtained. The vertical distances between each buoy and the target can be estimated correspondingly with the vector direction and its normal distance. Averaging over multiple buoys to remove the impact of waves can then be used to determine the estimation of the target depth D.

Similar to the projection scheme in [88], with the help of depth information, the underwater target and the surface buoys can be placed at the same plane approximately. Since the buoys are moving up and down in the Z direction, therefore, assuming the target and buoys' depths are 0 meters is an approximation, as shown in Figure 3.2. Moreover, the problem changes to a 2D localization problem. Define
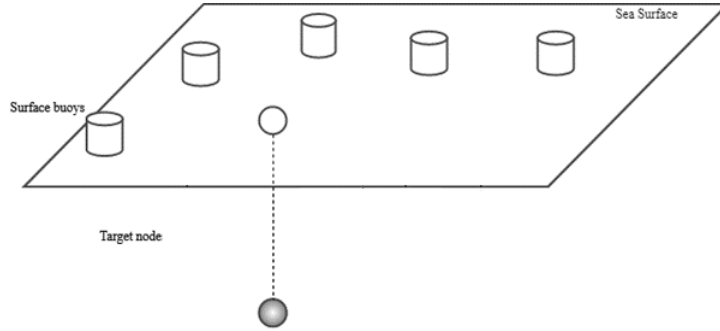
FIGURE 3.2: Projection diagram

the objective problem as:

$$\arg\min_{X} = \sum_{i=1}^{m}(\|X - B_i\| - \hat{d}_i)^2 \tag{3.10}$$

Where $X = (x, y)$ is the estimated coordinates of the target, and $B_i = (x_i, y_i)$, $i = 1, 2...m, (m > 3)$ is the coordinates of each buoy, where the number of buoys must greater than 3, or there would be two intersection points as shown in the Section 1.2. Denote $\hat{d}_i$ as the estimated distance of each measurement from step

42

one in Chapter 2. The goal of the 2D localization algorithm is to find a proper X, such that the objective function 3.10 can be minimized. The following section introduces two methods to solve the problem, Particle Swarm Optimization and the Majorization-Minimization approach.

Particle Swarm Optimization

Particle Swarm Optimization (PSO) [89] is a computational method that optimizes an objective function by iteratively finding the best candidate solution with regard to a given measure of quality. It uses several particles that consist a swarm searching around to find the best solution. Each particle keeps track of its own coordinates in the solution space, which is associated with the best solution (fitness) that has been achieved so far by that particle. This value is called personal best, *pbest*. The other best solution that the PSO tracking is the best value obtained so far by all particles in the neighbourhood of that particle. This value is called global best, *gbest*. The basic concept of PSO lies in accelerating each particle toward its *pbest* and the *gbest* locations, with a random weighted acceleration at each time step as shown in Figure 3.3 [5].

In the iterations, the same processes are carried out for each particle. Every particle p_i has a position X_i^t and a velocity V_i^t, which is used to update the particle's position in space. The position of the $i - th$ particle can be updated between iteration t and iteration $t + 1$ by using Equation 3.12.

$$X_i^{t+1} = X_i^t + V_i^{t+1} \tag{3.11}$$
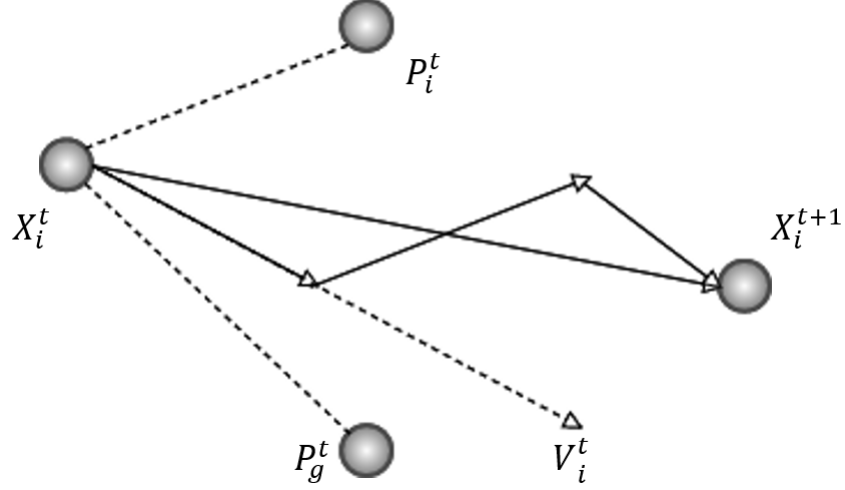
FIGURE 3.3: PSO characteristic [5]

In equation 3.12, X_i^t is the current coordinate of particle i and V_i^{t+1} is the velocity indicating the particle's next position. And t represents iteration index number. In each iteration step the velocity V_i^{t+1} is impacted by personal best location P_i^t and global best location P_g^t, show as the following equations:

$$V_i^{t+1} = WV_i^t + c_1 r_1 (P_i^t - X_i^t) + c_2 r_2 (P_g^t - X_i^t) \qquad (3.12)$$

Here, W is inertia weight, which is not kept fixed and is varied in the loop. In the simulation, W starts from 1 and is multiplied by a constant of 0.99 in each iteration. c_1 is the cognitive learning parameter, c_2 is the social learning parameter, according to [90], the appropriate learning parameters are $c_1 = c_2 = 2$, while r_1 and r_2 are random numbers uniformly distributed in the range [0,1]. Furthermore, the particle movement is restricted with maximum velocity to avoid jumping over the optimal location as per search requirements.

In the simulation, the initial point of the iteration is the average coordinate from all buoys. The population of particles is 10, and the maximum iteration times are set to 10 and 100. The results of using different iterations are compared in Chapter 4.

To estimate the coordinates of the underwater target, the process followed:

- The underwater target with at least four buoys in its transmission range L to be localized.

- Mean of coordinates of buoys falls within transmission range, considered as initial estimation position of the target node.

- Run the PSO algorithm and searches the global best solution as the estimated position of the target node.

Majorization-Minimization Approach

Majorization-Minimization Approach [91] is a way by transferring the non-convex problem to convex problem. The estimated distances including error obtained from step one in Chapter 2 can be written as $\hat{d}_i$, $i = 1, 2, ...m, (m > 3)$, where m is the number of buoys. Just as for the PSO algorithm, the goal is to minimize the objective problem:

$$\arg\min_X \sum_{i=1}^m (\|X - B_i\| - \hat{d}_i)^2 \tag{3.13}$$

where $X = (x, y)$ and $B_i = (x_i, y_i)$ are the coordinates of target and $i - th$ buoy in 2D space respectively. Expanding the square and dropping the constant term [92],

equation (3.13) equals to:

$$\arg\min_{X} \sum_{i=1}^{m} (\|X - B_i\|^2 - 2\hat{d}_i\|X - B_i\|) \tag{3.14}$$

which can be written as a sum of convex function and a concave function:

$$\arg\min_{X} \underbrace{\sum_{i=1}^{m} (\|X - B_i\|^2)}_{CVX(X)} + \underbrace{\sum_{i=1}^{m} (-2\hat{d}_i\|X - B_i\|)}_{CCV(X)} \tag{3.15}$$

where $CVX(X)$ denotes a convex function and $CCV(X)$ denotes a concave function. Clearly, Equation (3.15) is non-convex. In order to effciently compute this optimization problem, a surrogate function is constructed as the upper bound of the objective function 3.15 by using Majorization-Minimization (M-M) approach. In [93], a quadratic surrogate function $f(X^{t+1}|X^t)$is constructed by first order Taylor approximation, which leads to the concave function being upper bounded by a linear function:

$$CCV(X) \leq CCV(X^{(t)}) + \nabla CCV(X^{(t)})^T (X - X^{(t)}) \tag{3.16}$$

$$= -2\sum_{i=1}^{m} \hat{d}_i\|X^{(t)} - B_i\| - 2\sum_{i=1}^{m} \frac{\hat{d}_i(X^{(t)} - B_i)^T}{\|X^{(t)} - B_i\|}(X - X^{(t)}) \tag{3.17}$$

where T represents transpose and t represents iteration index number. Therefore, the objective function can be reformulated to:

$$f(X|X^t) = \sum_{i=1}^{m}(\|X - B_i\|^2 - 2\hat{d}_i\|X^{(t)} - B_i\|) - 2\sum_{i=1}^{m}\frac{\hat{d}_i(X^{(t)} - B_i)^T}{\|X^{(t)} - B_i\|}(X - X^{(t)})$$

(3.18)

$$X^{t+1} = \arg\min_X f(X|X^t)$$

(3.19)

in the iteration, let

$$\nabla f(X^{(t+1)}|X^{(t)}) = 0$$

(3.20)

then

$$X^{(t+1)} = \frac{1}{m}\sum[B_i + \frac{\hat{d}_i(X^{(t)} - B_i)}{\|X^{(t)} - B_i\|}]$$

(3.21)

where X^{t+1} is the result after iterations. Since the original problem is non-convex, to prevent the result converging to a local optimum, the author in [94] used the linear least square method with discarding the quadratic constraint to calculate

the iteration initial point, define the $X_{initial}$ as:

$$X_{initial} = (A^T A)^{-1} A^T b \tag{3.22}$$

where

$$A = \begin{bmatrix} -2B_1^T & 1 \\ \vdots & \vdots \\ -2B_m^T & 1 \end{bmatrix} \tag{3.23}$$

$$b = \begin{bmatrix} \hat{d_1}^2 - \|B_1\| \\ \vdots \\ \hat{d_m}^2 - \|B_m\| \end{bmatrix} \tag{3.24}$$

Iterations of the algorithm are run to search for the global best solution as the estimated position of the target.

Complexity Discussion

For the PSO algorithm, the computational time complexity depends on the maximum number of iterations t_{max}, the total number of particle populations p and the number of buoys, m. Assuming that each particle needs to run for $O(n_1)$ time per iteration, then the total time can be expressed as $O(t_{max} \times p \times n_1 \times m)$. Similarly, if the computational time complexity needed for each buoy in LS method is $O(n_2)$, then the total computation time for LS method is $O(m \times n_2)$. In addition, in the M-M approach, the iteration process starts from the solution of LS method. If

each iteration of the MM algorithm requires $O(n_3)$ time, the computation time for the M-M approach can be simply denoted by $O(n_2) + O(m \times i \times n_3)$, where i is the iteration times.

3.2 Adaptive time slot

In the application scenarios described, the target is moving at high speed on the order of 100 m/s. It is assumed that at least ten buoys are used to transmit signals one after another at the same wavelength, as shown in Figure 3.4. However, the signals are not distinguishable from different buoys. Surface transmitters can receive GPS signals, such that time synchronization can be achieved.
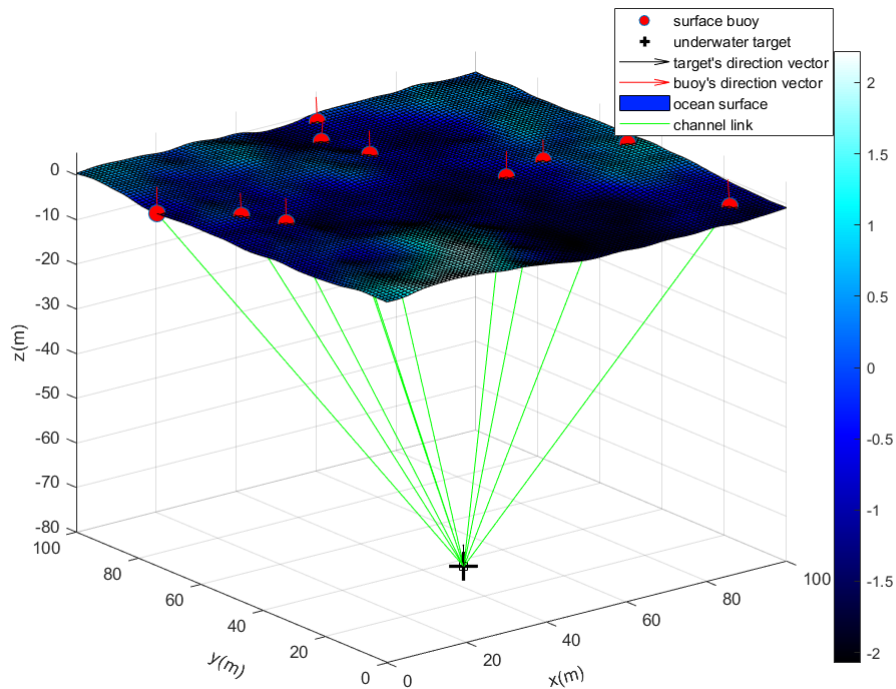

FIGURE 3.4: Randomly deployed buoys and one underwater target.

3.2.1 Time slot definition

As shown in Figure 3.5, the signal time duration T transmitted from each transmitter is regarded as one time slot, e.g. T_i is the time interval of the i-th signal, where red and blue represent two adjacent signals' time intervals. When all the buoys continuously transmit signals one after another, these ten time slots form a time sequence at the transmitter side from $t = 0\mu s$ to $t = 100\mu s$. And they have no time overlap. It is assumed that when the target exceeds the maximum emission angle of 65° of the LED source or the target is more than 100m away from the buoy, the target cannot receive the signal. The time slot is set to empty correspondingly. At the receiver side, the target gets the signal interval with time delay t_i due to the propagation time, where t_i is given by the following equation:

$$t_i = \frac{d_i}{\frac{c}{n}} \tag{3.25}$$

where c is the speed of light in the vacuum and n is the seawater refractive index. For instance, the i-th signal interval T_i is shifted because of t_i. It is assumed the receiver has the ability to detect the rising of the received power level, and its clock will automatically start counting T time to calculate the received power within the interval. However, because the buoys are randomly deployed, the distances between the buoys and the target are not equal. In other words, the underwater propagation time of each buoy's signal is not equal to each other, which may lead to discontinuity, overlap, or loss of the received signals at the receiver side.
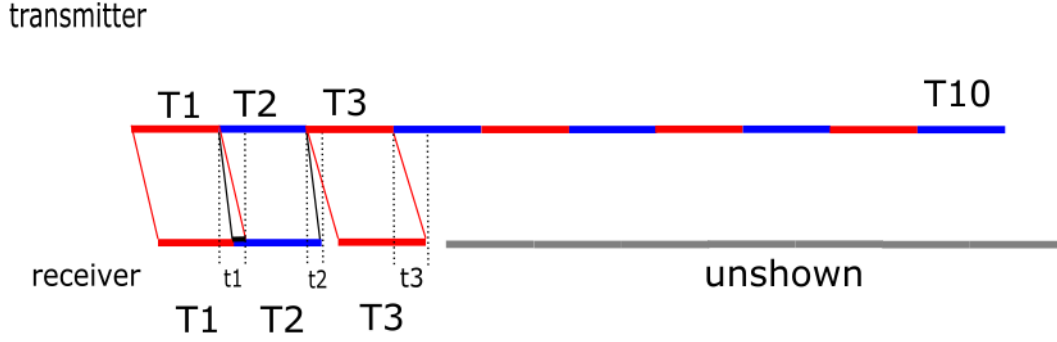
transmitter

FIGURE 3.5: Time slots' duration T with different time delay $ti, i = 1, 2, ...m$, where m is the number of buoy.

3.2.2 Time slot overlap situations

In Figure 3.5 an example is illustrated, at the transmitter side, three buoys continuously transmit signals without overlap or gap. Due to the different distances to the target, the signal propagation times are represented as $t1$, $t2$ and $t3$. If the buoys are equidistantly distributed around the target, then the light propagation times of all the transmitters are equal. In this situation, when the target receives the signal from the first buoy for T_1 time with time delay t_1, the next received signal interval T_2 with a time delay t_2. Clearly, $t_2 = t_1$, as a result, two signal intervals at the receiver side have the same shift. Thus, the second signal interval T_2 will be completely from the second buoy without any overlap.

However, if the second buoy is closer than the first and the third buoys to the target as shown in the number (4) of the Figure 3.7, then $t2 < t1$ and $t2 < t3$, when the receiver starts to calculate the energy from the first buoy, it will also receive the signal interference from the second closer buoy, which causes errors when calculating the distance through the LED Lambertian Equation 2.34 introduced

in Chapter 2. Similarly, when calculating the optical energy from the second buoy, not only the optical energy from the first buoy should be taken into account, the optical energy from the third buoy should be considered as well if the third buoy is farther than the second, propagation time $t3 > t2$. As a result, the third buoy will not affect the second buoy and vice versa.

When studying the energy sources within a time slot, only its previous time slot and the next time slot need to be considered. Hence, only three time slots need to be discussed each time. Simply, name their time slots $T1, T2$ and $T3$ respectively, and their propagation time delay $t1$, $t2$ and $t3$. Compare the value of $t2$ with $t1$ and $t3$ to determine whether the second time slot is affected by the previous or the next time slots. However, there is no previous time slot for the first one ($T1$) or next time slot for the last one($T10$); therefore, two null time slots $T0$ and $T11$ with zero optical power are added on both sides of the receiver time sequence as shown in 3.6.
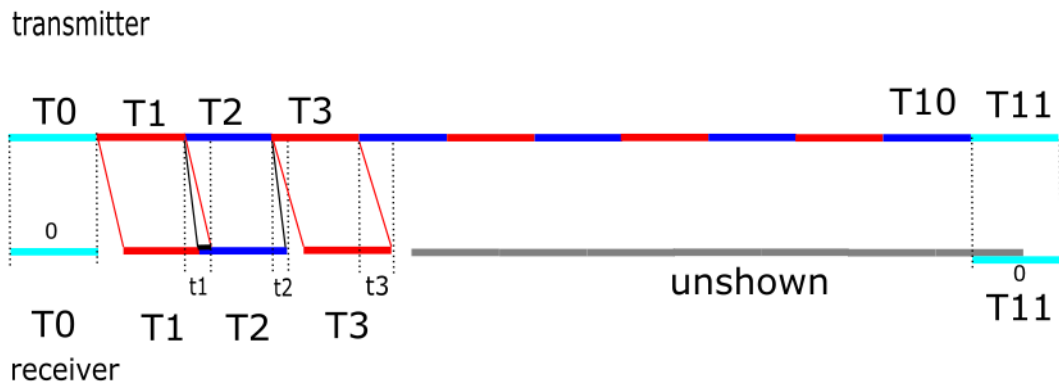

FIGURE 3.6: $T0$ and $T11$ are represented by green time slots with zero optical power, which means they will not interfere with other time slots.

The example in Figure 3.5 and Figure 3.6 is one possible situation. Figure 3.7 lists all nine possible situations of buoys geometry positions. Because only three buoys' signals in the continuous-time need to be considered each time, only three buoys are shown in each situation in the figure. In other words, the interference of the previous buoy (B1) and the next buoy (B3) should be considered each time. In each row of the 9 subfigures, the influence of the previous buoy (B1) on the current buoy (B2) is the same. In each column, the influence of the next buoy (B3) on the current buoy is the same.

In Subfigures (1), (2) and (3), the signal of B1 exceeds the maximum emission angle, or the transmitter is more than 100m away from the target, so its signal will not be received at all, which means that the signal B1 will not interfere with B2. In Subfigure (1), B3 is further than B2, therefore $t3 > t2$, there will be no power interference from the third buoy. In Subfigure (2), when B3 is closer to the target than B2, $t2 > t3$, there will be some light power interference from B3 when calculating the current buoy's signal power. Nevertheless, when B3 is also far away or its signal exceeds the maximum emission angle, its signal power is determined to be 0, as shown in Subfigure (3). In Subfigures (4), (5), and (6), the previous buoy B1 is farther than B2, so the signal propagation time is longer. When calculating the signal power of the current buoy B2, there will be signal interference from B1. As for the B3, situation (5) and situation (6) are similar to case (2) and case (3). In Subfigures (7), (8), and (9), the previous buoy B1 is closer to the target with a shorter signal propagation time, so even with time delay, the time slot $T1$ will not affect the current buoy B2. Note that cases (8), (9) are similar to cases (2) and (3) in terms of the third buoy.

Correspondingly, Figure 3.8 shows nine overlap situations of time slots. The time slots are represented by the blue bars. The signal duration is T. If the buoy is too far away or the signal exceeds the maximum emitting angle, the signal power in the time slot is determined to be 0. If the signals of two buoys at adjacent times do not overlap, there will be a gap between their time slots and vice versa. For example, in case (1), B1 is far away from the target, and B3 is also farther than B2. Therefore, the optical power of the first time slot is set to be 0, and there is no power overlap between time slot $T2$ and $T3$. In contrast, case (5) shows the most complicated situation, where B2 is closer than B1, and B3 is closer than B2. As a consequence, the second time slot is influenced by both $T1$ and $T3$.
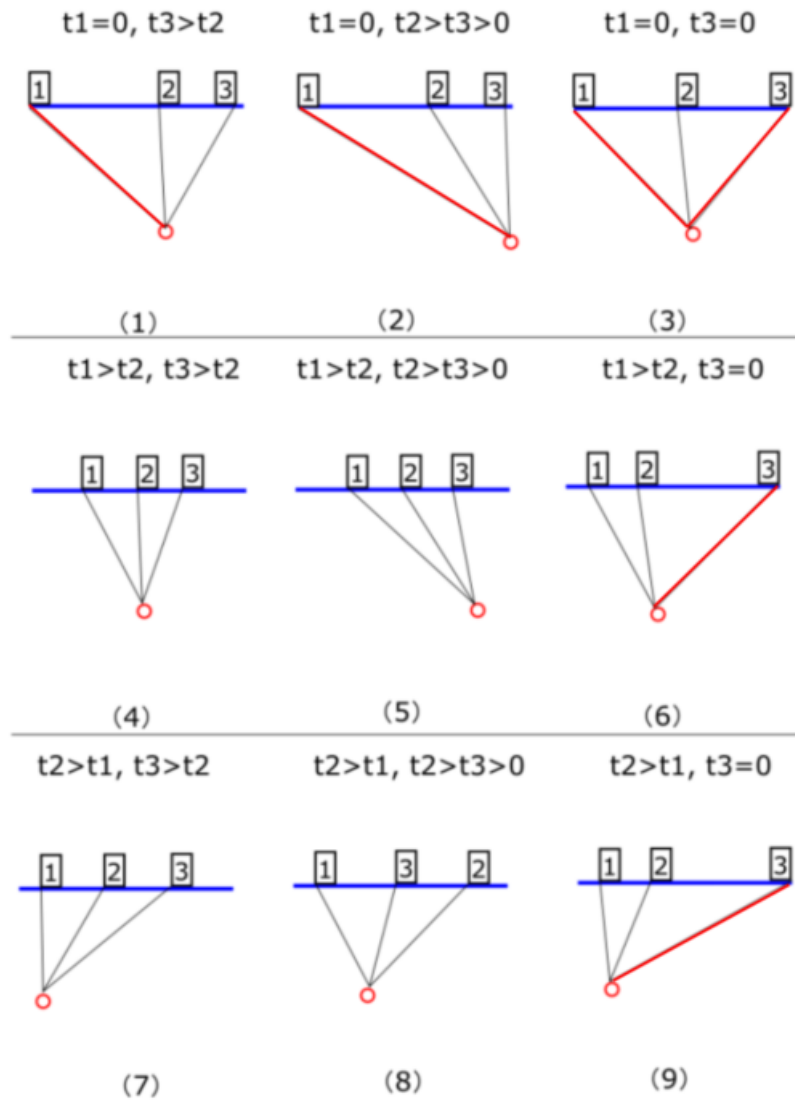
FIGURE 3.7: 9 different overlap situations, the numbers in the square represent three buoys B1, B2 and B3 in continuous time, the red circle represents underwater target and red line represents channel link out of range.

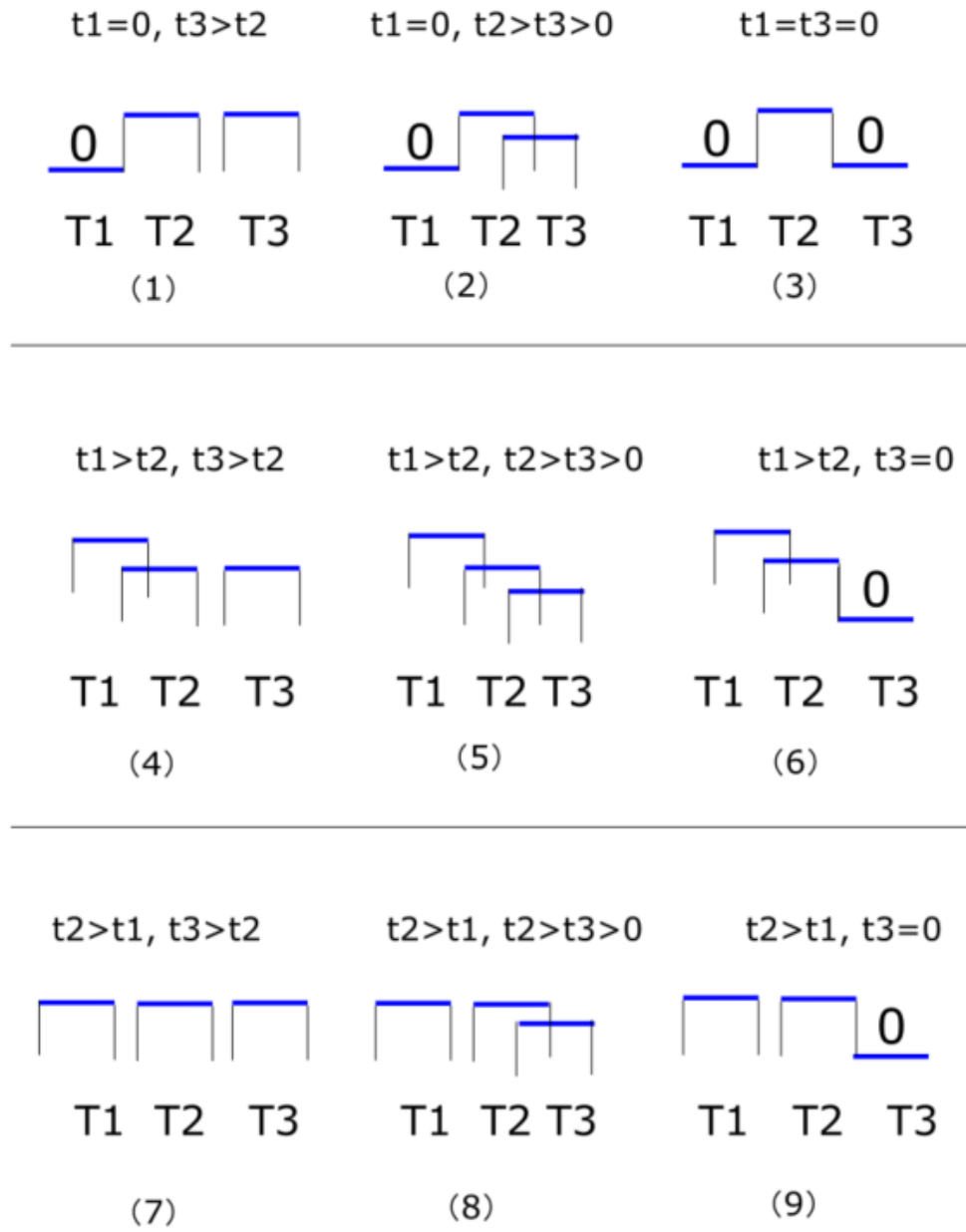FIGURE 3.8: 9 different situations, signals' power overlap are illustrated

3.2.3   Time slot update

Because there may be signal interference from other buoys to the current time slot
as shown in the Figure 3.8, so the estimated distance $\hat{d}$ calculated by the LED
Equation 2.34 within the current time slot may contain errors. After using the
LS method, PSO or M-M localization algorithms introduced in Chapter 3, the
estimated position may contain errors as well. Therefore, this thesis proposes an
adaptive time slot approach, which is a secondary distance optimization based
on the first estimated distance $\hat{d}$. The first estimated position can provide an
approximate signal propagation time t'_i. Then, according to the relationship among
all these propagation times $(t'_1, t'_2, ...t'_{10})$, the time overlap in each situation can be
determined. After that, the time slots can be adjusted to remove the optical
interference power from other buoys approximately.

   An example is shown in Figure 3.9. It is assumed that the previous buoy
(B1) is far away from the target with zero optical power, whereas the next buoy
(B3) is closer than the current buoy (B2), and their light propagation time are $t2$
and $t3$, respectively, as shown in Subfigure (1). Therefore, there is a little power
interference from B3, the overlap of their time slots represented by $tt = t2 - t3$,
and the received light power within the time slot can be expressed by:

$$p2' = \frac{p2 \times T_2 + p3 \times tt}{T} \tag{3.26}$$

$$p3' = \frac{p3 \times T_3 + p2 \times tt}{T} \tag{3.27}$$

where $p2$, $p3$ are the optical power over interval T without overlap, and $p2'$, $p3'$ are
the optical power containing overlap parts. Based on the $p2'$, $p3'$ and other optical
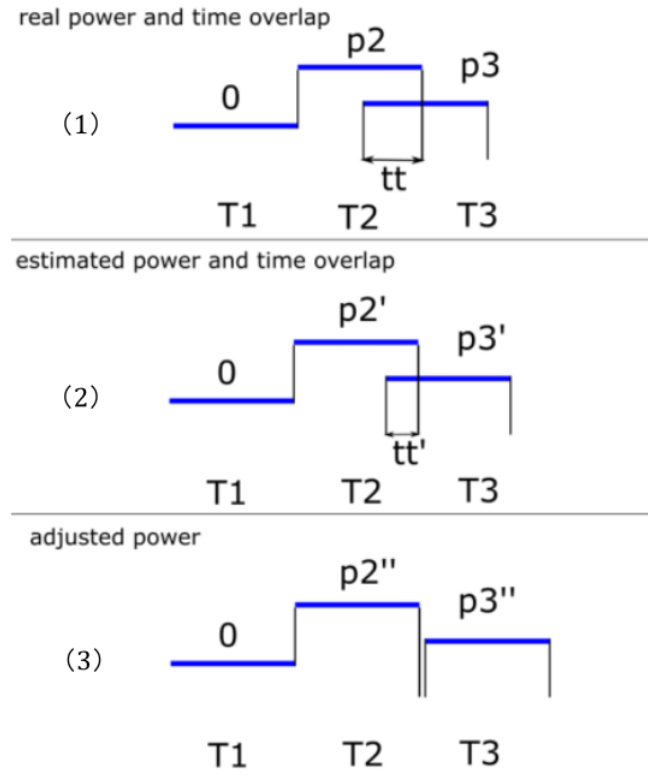
FIGURE 3.9: remove power overlap using adaptive time slot

power, the estimated distances and estimated position can be obtained. Then regard the estimated position as a given condition, the estimated propagation time $t2'$, $t3'$ and time overlap $tt' = t2' - t3'$ can be calculated, as shown in Subfigure (2). In the final step, the optical power over the time tt' from both $T2$ and $T3$ need to be removed:

$$p2'' = \frac{(p2' \times T_2) - (p3' \times tt')}{T} \tag{3.28}$$

$$p3'' = \frac{(p3' \times T_3) - (p2' \times tt')}{T} \tag{3.29}$$

where $p2''$ and $p3''$ are the updated optical power. A more accurate estimated

position can be obtained with the updated optical power. However, the estimated parameters including power, distances, propagation time and time overlap are all containing errors, which means the interfered power can only be removed approximately, not accurately. Numerical results are shown in Chapter 4.

3.2.4 Discussion

In the assumption, the localization algorithm needs to wait 10 time slots to start. Therefore the latency is determined by the number of buoys. For example, if ten buoys are used, then the latency is $100\mu s$, the movement of the target is 0.01m, and the speed of the target is 100m/s. However, when a larger group of buoys is used the latency and the movement of the target can be higher. Additionally, after the first round of measurements, the process repeats. Therefore, the rate of localization depends inversely on the number of buoys and the time interval of the time slot. In addition, with a smaller group of the buoys, e.g., the number of buoys is 10, if a small time gap between successive emissions is inserted, the power overlap can be neglected. Nonetheless, in the real situation, the sea area may be on the scale of kilometres. In that case, a larger group of buoys may be required. The total time from time slot and time gap over all the buoys may lead to the non-negligible error to the target's position. There are several strategies that could be used to reduce the waiting time due to the large group of buoys. For example, the area can be divided into smaller zones, and the target can select some of the prior buoys that belong to the closer zone.

3.3 Chapter summary

This chapter introduces underwater localization algorithms, including the 3D Least square method, 2D Particle swarm optimization and Majorization-minimization. Explains how to transform a three-dimensional localization problem into a two-dimensional space problem. The concept of time slot and adaptive time slot is illustrated, and the process of removing interfered optical power is also explained. The numerical results are shown in Chapter 4.

Chapter 4

Numerical Results

Results accuracy of the localization algorithms introduced in Chapter 3 is numerically evaluated in this chapter, including the 3D LS method, PSO and M-M approach. The root means square error (RMSE) as a metric is used to compare their accuracy under two scenarios. In the first scenario, buoys are deployed randomly, while in the second scenario, there is a 9-buoy fixed scheme. The proposed adaptive time slot (ATS) introduced in Section 3.2 is used in both scenarios. Matlab is used to generate a $100m \times 100m \times 80m$ sea area and a 3D ocean surface using the P-M spectrum presented in Chapter 2. Simulation parameters used in all simulations in this chapter are presented in Table 4.1. Table 4.2 summarizes the key assumptions made in computing these numerical results as discussed in Chapter 2 and Chapter 3.

Parameter	Value
surface model starting time	$t = 100$
time interval	$\Delta t = 0.1$
number of wave circular frequencies ω	N = 10
number of wave direction angles θ	M = 8
speed of wind $U_{19.5}$	15 m/s
height of average sea level	0 meter
simulation area (X,Y,Z)	$100m \times 100m \times 80m$
maximum link distance	100 m
LED maximum emitting angle	65°
LED bandwidth and power	532 nm and 20 w
LED Lambertian semi-angle at half power	65°
diffuse attenuation coefficient K_d	$\approx 0.0519m^{-1}$ (pure sea water)
receiver FOV	180°
particle population in PSO	10
maximum iterations in PSO	10 and 100
maximum iterations in M-M approach	10
underwater target speed	$100m/s$
time slot duration	$T = 10\mu s$

TABLE 4.1: Simulation parameters

Assumptions
1. The optical filter can reject background noise and sunlight
2. There is no receiver noise
3. There are no GPS errors
4. Pure seawater is used, scattering effect can be neglected
5. The buoys only move up and down with sea surface
6. Signals propagating in excess of 100m will not be received
7. Signals exceeding a maximum emission angle (65°) will not be received
8. The sea waves satisfy the Gaussian stochastic process and is a fully grown wave
9. LED transmitters follow LED Lambertian pattern
10. Gyros are used on both buoys and the target to provide altitude information
11. A light direction sensor is used on the receiver
12. The computation time for the localization algorithm is not significant

TABLE 4.2: List of Key Assumptions

4.1 Scenario 1 - Randomly deployed Buoys and Target

As introduced in Chapter 3, the adaptive time slot (ATS) concept is designed to improve localization accuracy. In this scenario, ten randomly deployed surface buoys send light signals one by one continuously. Recall there is no time gap between any of the buoys signals aided by GPS synchronization. One underwater target is also randomly deployed near the bottom of the simulated sea area. The depth of the target is a single uniformly distributed random number in the interval (-80 m,-70 m), as shown in Figure 4.1. The localization algorithm results are compared among the 3D LS method, PSO algorithm and M-M approach described in Chapter 3. For realism, a maximum 2° angle error in the LED Lambertian channel is added, as mentioned in Chapter 2. This section uses Matlab [95] to run the simulation 10000 times with random positions of buoys, target, and ocean surface in each simulation time. This section also compares the RMSE results before and after using the ATS concept among three different localization algorithms in the following figures (Figure 4.2, Figure 4.3, Figure 4.4, 4.5, 4.6 and 4.7). Table 4.3 summarizes the comparison results, including RMSE, mean and variance of error in each case.

Figure 4.2 and Figure 4.5 show a comparison of performance with and without ATS obtained by Matlab CDF (Cumulative Distribution Function) function over 10000 times simulations. Any spatial distance exceeding $100m$ is regarded as invalid data and deleted. The improved localization accuracy can be found in LS and M-M algorithms; the RMSE before using the ATS are 14.4 m and 0.28
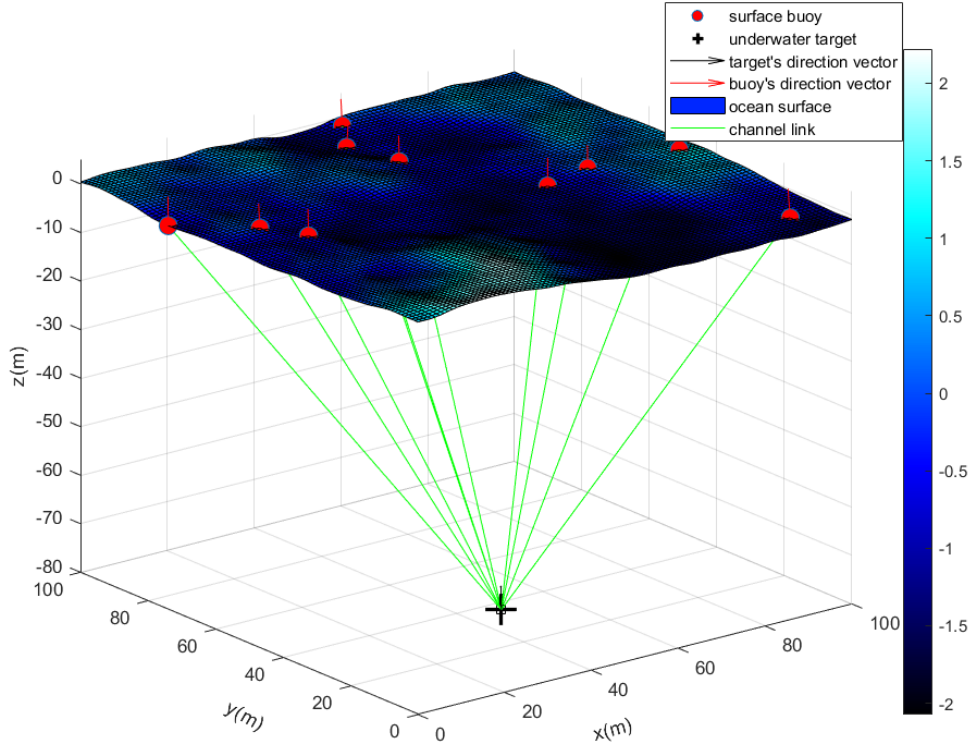
FIGURE 4.1: scenario 1: randomly deployed buoys and target

ten buoys	LS	PSO-10	PSO-100	M-M
RMSE (no ATS)	14.2 m	1.89 m	1.48 m	0.28 m
RMSE (with ATS)	4.4 m	1.85 m	1.36 m	0.04 m
improvement RMSE (%)	68%	2%	8%	82%
mean (no ATS)	7.6 m	1.30 m	0.49 m	0.23 m
mean (with ATS)	0.55 m	1.28 m	0.27 m	0.03 m
variance (no ATS)	143 m^2	1.90 m^2	1.95 m^2	0.03 m^2
variance (with ATS)	19.2 m^2	1.80 m^2	1.79 m^2	0.001 m^2

TABLE 4.3: Comparison of results among LS, PSO and M-M localization algorithms.

m, respectively, whereas the ATS results are 4.4 m and 0.04 m. In these two algorithms, the positioning accuracy has been improved significantly, which are 68% and 82% respectively. As illustrated in Section 3.1.2, the initial point of the
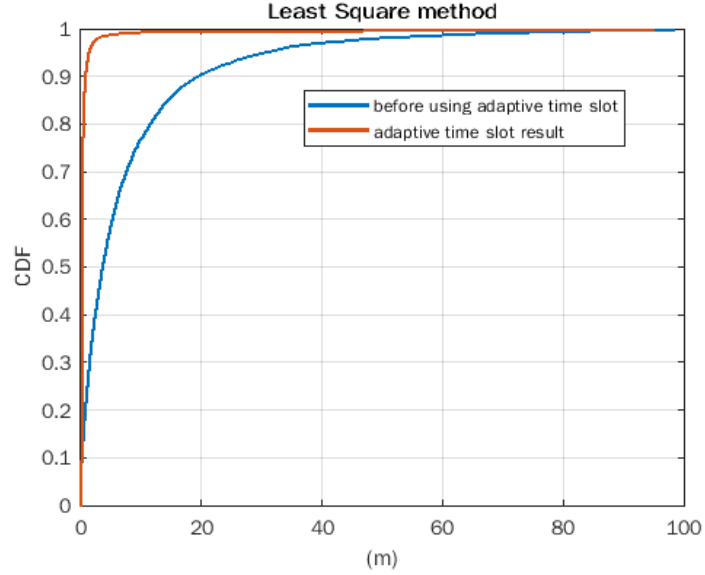
FIGURE 4.2: Comparison of results before and after using ATS,
where 3D LS method is adopted during 10000 times simulations.

M-M approach is set to

$$X = (A^T A)^{-1} A^T b$$

, which is similar to the estimated result of the LS method described in Section
3.1.1. However, the M-M approach uses the initial point as the start point in the
iteration to find a more optimum solution as shown in Equation 3.21 and Equation
3.22. Therefore, the M-M approach can provide more accurate results.

However, in Figure 4.3 and Figure 4.4, the positioning accuracy of the PSO
algorithm has not been significantly improved with the use of ATS. When the
iteration of the PSO algorithm is set to 10, the CDF curves before and after using
ATS are nearly overlapped in Figure 4.3, and the accuracy is only improved by
2%. This phenomenon is because those twice searches start from the same initial
point (the geometric center of the buoys' position) when the number of iterations
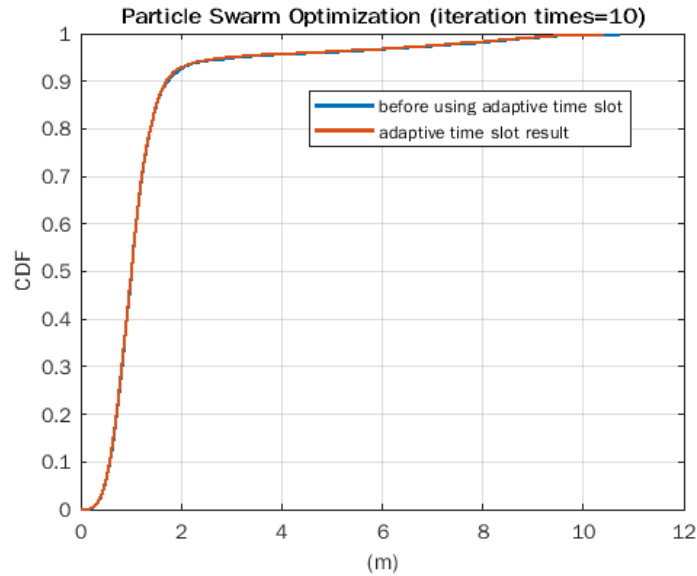
65

FIGURE 4.3: Comparison of results before and after using ATS, where 2D PSO (iteration times = 10) is adopted during 10000 times simulations.

is small; even if the adaptive time slot concept is used, a much better result cannot be found. When the number of iterations is set to 100, the accuracy is increased by 8% after using the adaptive time slot in Figure 4.4. In addition, when the number of iterations is increased, the positioning accuracy of the PSO algorithm itself is also improved, RMSE (before) decreasing from 1.89 m to 1.48 m and RMSE (after) decreasing from 1.85 m to 1.36 m, respectively.

The RMSE results among three localization algorithms are also compared in Figure 4.6 and Figure 4.7. In general, the M-M approach has the highest positioning accuracy. Regardless of whether the ATS is used, the RMSE error has a probability of more than 90% to be within half a meter. Before using the ATS method, results show that the M-M approach is better than PSO-100, better than PSO-10, and better than LS. The error of the PSO-100 algorithm has more than

FIGURE 4.4: Comparison of results before and after using ATS, where 2D PSO (iteration times = 100) is adopted during 10000 times simulations.

90% of the probability less than 1 m, and the PSO-10 algorithm has more than 90% of the probability less than 2 m before the ATS is used. After using the ATS method, PSO-100 is closer to the result of the M-M approach, but it has approximately 3% of possibility that error larger than 5 m. As a result, it has a slower rise in the error interval greater than 2 m than the LS algorithm with ATS.
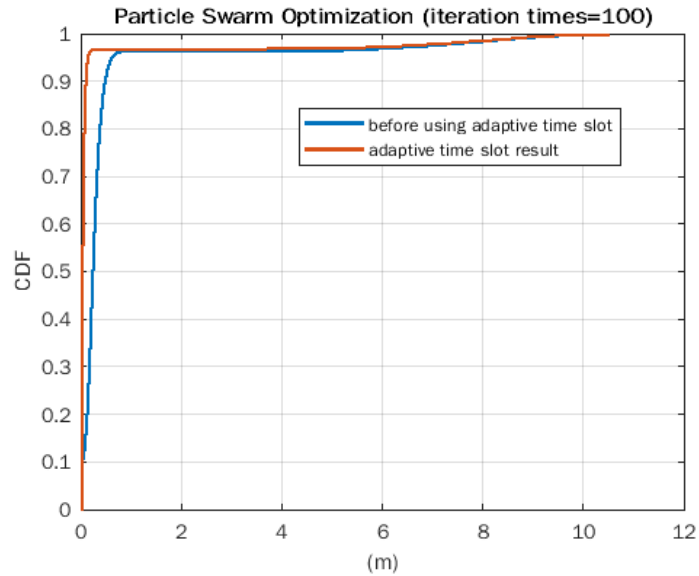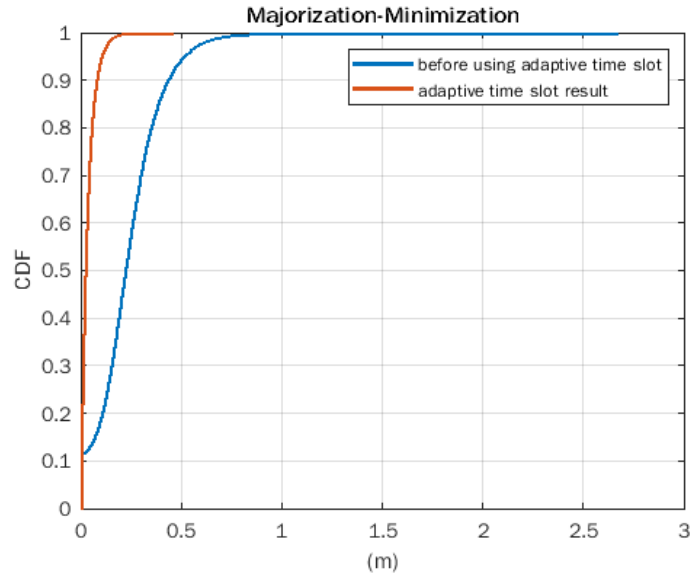
FIGURE 4.5: Comparison of results before and after using ATS, where 2D M-M approach (iteration times = 10) is adopted during 10000 times simulations.

FIGURE 4.6: Comparison of different localization algorithms' results before using the ATS, where PSO-10 and PSO-100 represent the number of iterations equal to 10 and 100, respectively.

FIGURE 4.7: Comparison of different localization algorithms' results after using the ATS, where PSO-10 and PSO-100 represent the number of iterations equal to 10 and 100, respectively.

4.2   Scenario 2 - Fixed 9-Buoy distribution scheme

In the second scenario, a practical situation to localize the underwater target
with buoys is proposed as the 9-buoy distribution formation as shown in Figure
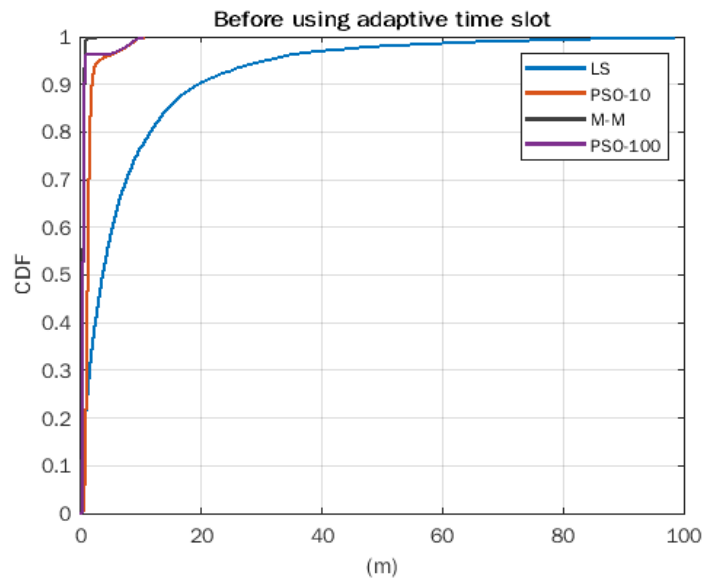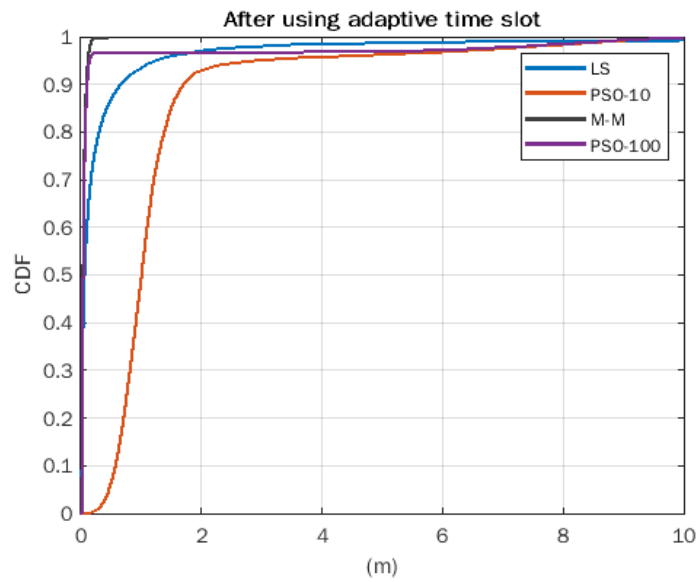4.8. Assuming that nine buoys are anchored to the seafloor at the given posi-
tions of the simulation surface with 25-meter intervals horizontally and vertically,
$x, y \in [25, 50, 75]$. Using the same sea surface model as the first scenario. However,
two cases are introduced in this section. The first case is a fixed 9-buoy distribu-
tion is used with a randomly deployed target, which localization accuracy can be
compared with the first scenario in Section 4.1. In the second case is the target
deployed at a given position with various depths, and the RMSE error distribution
is presented in Subsection 4.2.2.
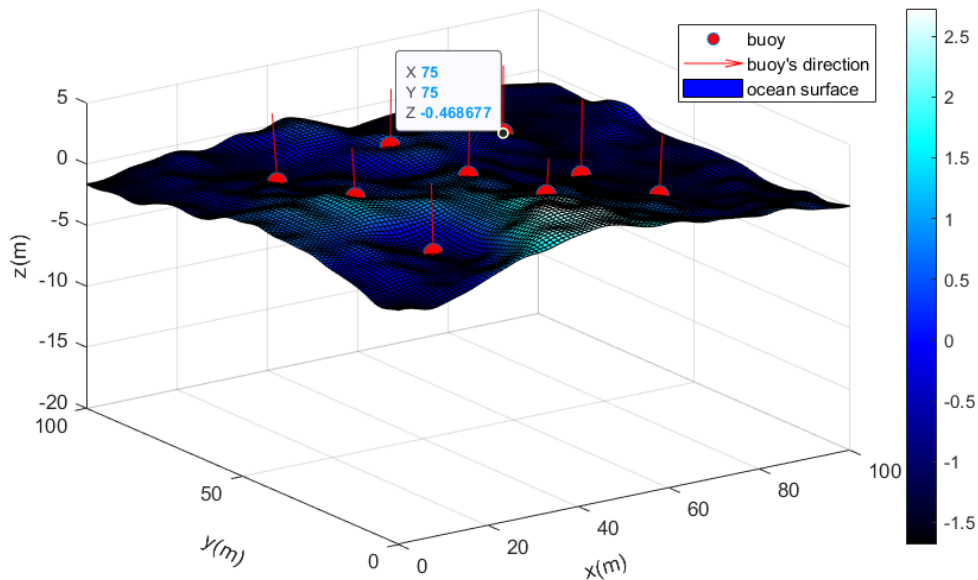
FIGURE 4.8: Scheme 2. Fixed 9-buoy distribution scheme

4.2.1 Randomly deployed target

Same as the first scenario described in Section 4.1, one underwater target is randomly deployed near the bottom of the simulated sea area shown in Figure 4.9, where depth is a single uniformly distributed random number in the interval (-80 m,-70 m). Matlab is used to run the simulation 10000 times under the situation. The RMSE error, mean and variance of error are compared with randomly deployed ten buoys scenario, results are summarized in Table 4.4.

FIGURE 4.9: 9-buoy distribution scheme with randomly deployed target

When comparing the two Tables 4.4 and 4.3, it is found that the accuracy of the M-M algorithm is the highest in both scenarios and does not vary a great

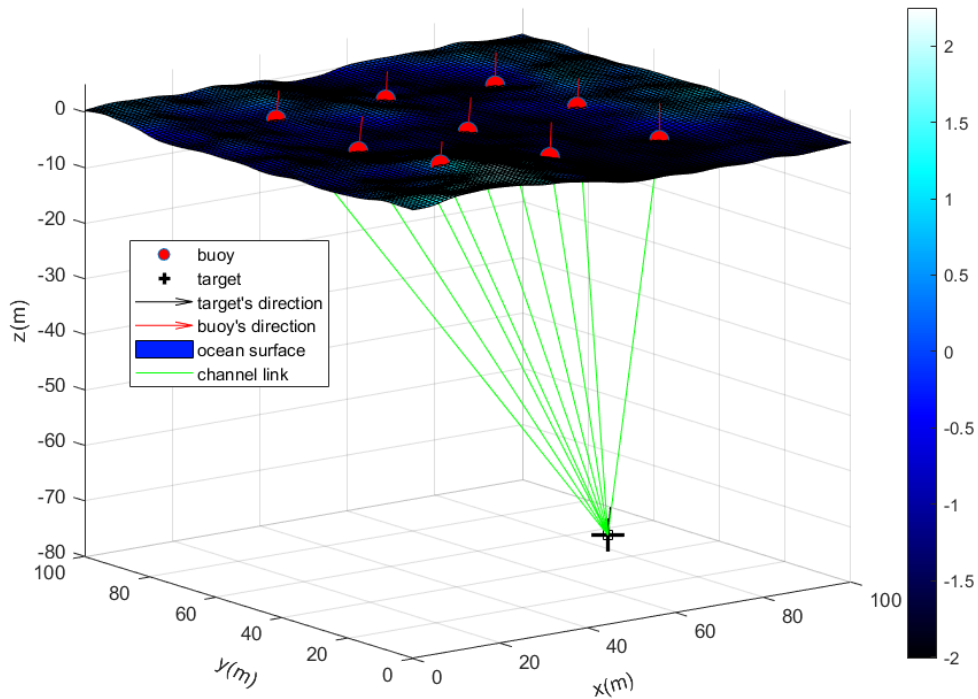| 9-buoy	LS	PSO-100	M-M
RMSE (no ATS)	6.34 m	0.57 m	0.24 m
RMSE (with ATS)	3.96 m	0.42 m	0.06 m
improved RMSE (%)	37%	25%	75%
mean (no ATS)	2.5 m	0.24 m	0.21 m
mean (with ATS)	0.45 m	0.07 m	0.05 m
variance (no ATS)	36.3 m^2	0.27 m^2	0.02 m^2
variance (with ATS)	18.4 m^2	0.18 m^2	0.002 m^2

TABLE 4.4: Comparison of results among LS, PSO and M-M localization algorithms under 9-buoy distribution scheme.

deal. However, the PSO and LS algorithms have higher positioning accuracy in the second scenario as compared to scenario 1. Before using ATS, the RMSE between scenarios 1 and 2 of the LS method decreased from 14.4 m to 6.34 m, and after using ATS, the RMSE results decreased from 4.4 m to 3.96 m. The RMSE results of the PSO algorithm show a similar trend. In general, placing buoys in the fixed 9-buoy distribution scheme can achieve higher positioning reliability. In this way, the given buoy's position formation can reduce the signal power overlap caused by random distribution, so the positioning error is relatively smaller.

4.2.2 Fixed depth

In the second case, every point on the $X - Y$ plane at fixed depth (-80 m, -60 m and -40 m) from $(x = 0, y = 0)$ to $(x = 0, y = 1)$, $(x = 0, y = 2)$, ..., and in the end $(x = 100, y = 100)$, which can be seen as the fixed position of underwater target. The minimum depth is underwater -40 m, and there will be no results if the target gets closer to the surface due to the maximum emission angle (65°) of the LED source. Matlab is used to run the simulation three times at each given target's position, and the RMSE error of every single point forms an error distribution

map at a given depth as shown in Figures 4.10, 4.11 and 4.12. Any RMSE results exceeding $100m$ are regarded as invalid data and are deleted. In the four corners of

FIGURE 4.10: RMSE of every point on the Z = -80 m plane under 9-buoy distribution scheme, subfigures in the first row are the results before using ATS and second row of subfigures are the results used ATS.

the simulation area (i.e., near (0,0), (0,100), (100,0) and (100,100)), far away from the buoys' location, the RMSE error is larger than in the central area, and more buoy signals can be received in the center of the simulation area, so the positioning result is ideal. Compared with the other two algorithms, the positioning results of the LS algorithm have a larger error. When the depth is -40 m, some RMSE results in the corner area are larger than $100m$, which are invalid and are deleted. Therefore, the coverage area under the LS algorithm at -40 m is smaller than at -60 m and -80 m. Moreover, the RMSE error of the PSO algorithm is closer to that of the M-M approach at depth -40 m and -60 m.
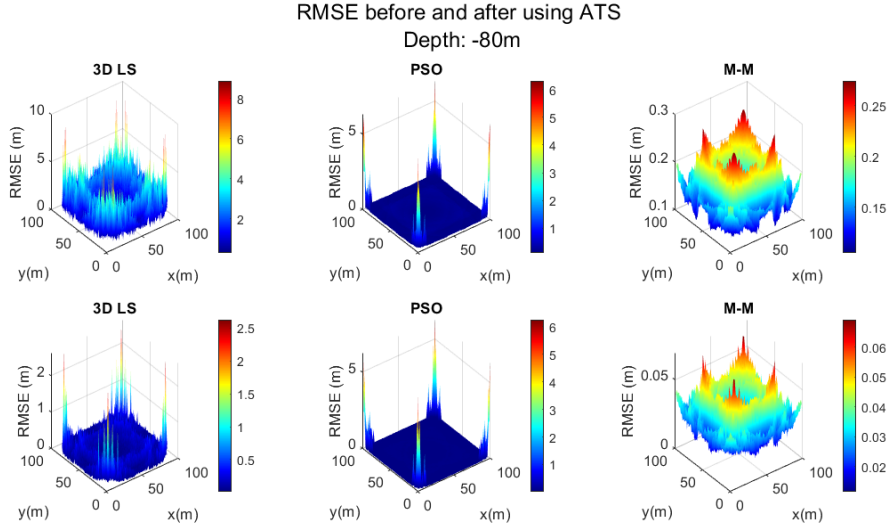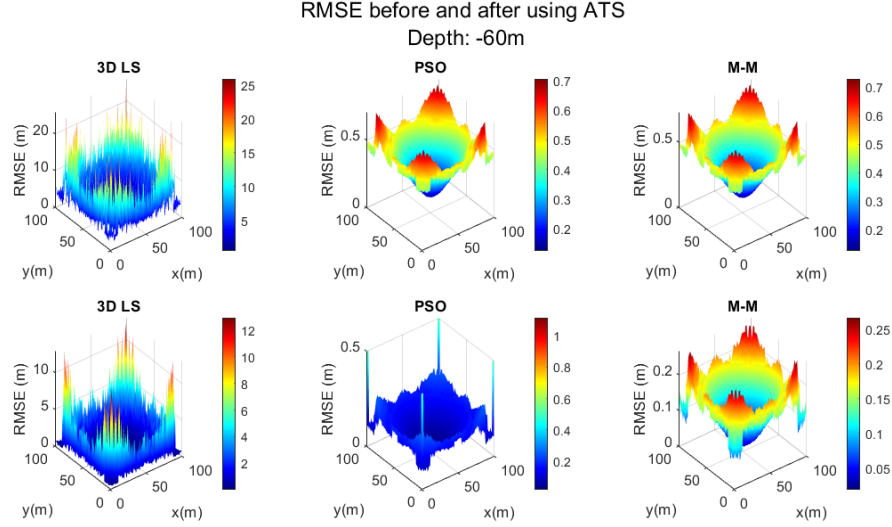
FIGURE 4.11: RMSE of every point on the Z = -60 m plane under 9-buoy distribution scheme, subfigures in the first row are the results before using ATS and second row of subfigures are the results used ATS.

The ATS results also improve the localization reliability among the three algorithms, as shown in Figures 4.13, 4.14 and 4.15. The CDF curve after using the ATS approach shows a larger slope compared with the ones before using it. However, it is not difficult to find that in Figure 4.13, the CDF curve at -40 m cannot be integrated to 1 because many error data have been deleted, which means the coverage area that the target can be positioned at a depth of -40 m is smaller than the other two depths. Furthermore, in each case, the slope of the CDF curve gradually becomes flat as the depth decreases. This is due to the interference from other buoys' optical signals increasing, resulting in a decrease in the positioning accuracy among the three localization algorithms. The mean of RMSE errors summarized in Table 4.5 can also show this behaviour. Notice that no background noise or other noises are considered in the simulation, which should be discussed in future work.
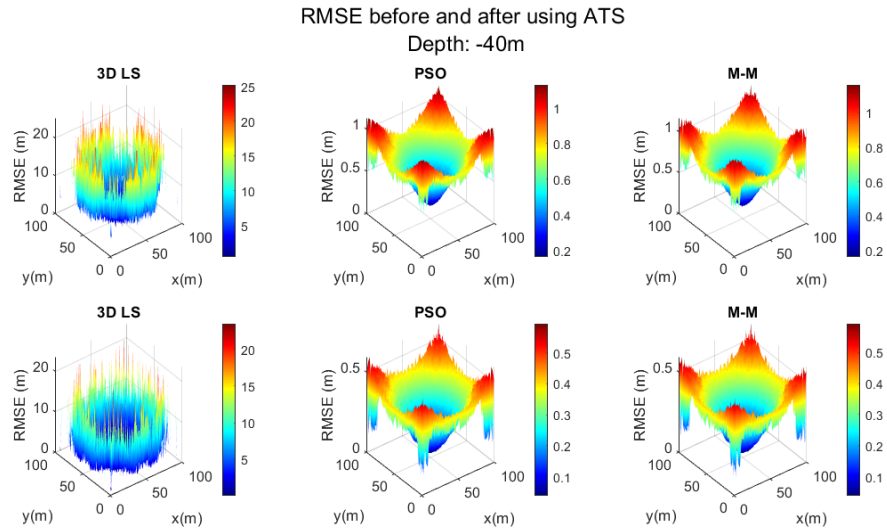
FIGURE 4.12: RMSE of every point on the Z = -40 m plane under 9-buoy distribution scheme, subfigures in the first row are the results before using ATS and second row of subfigures are the results used ATS.

Depth	LS	PSO-100	M-M
-80 m	1.55 m	0.19 m	0.17 m
	0.13 m	0.06 m	0.03 m
-60 m	4.45 m	0.40 m	0.40 m
	1.14 m	0.13 m	0.129 m
-40 m	7.8 m	0.66 m	0.67
	4.3 m	0.302	0.302

TABLE 4.5: Mean of RMSE errors under 9-buoy distribution scheme with different depths.
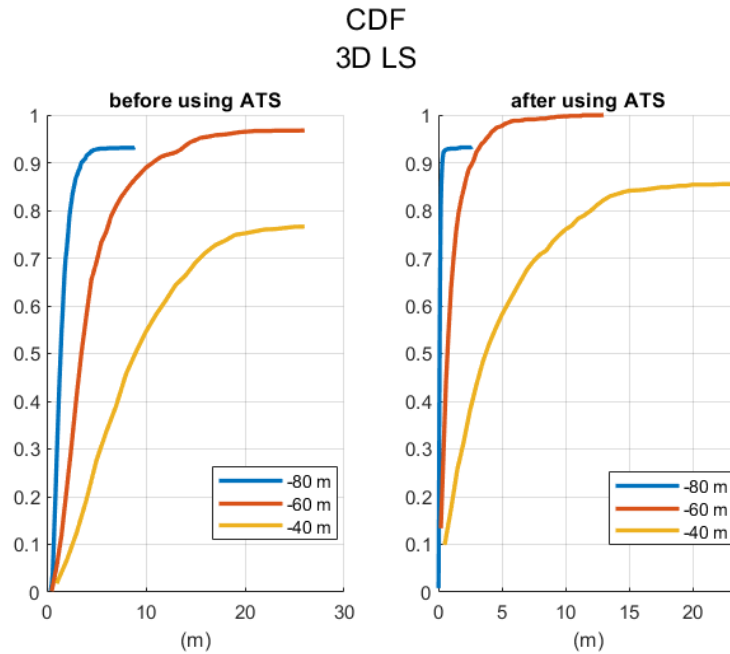
FIGURE 4.13: Cumulative distribution function of RMSE error changing with depth while using LS algorithm

FIGURE 4.14: Cumulative distribution function of RMSE error changing with depth while using PSO-100 algorithm

FIGURE 4.15: Cumulative distribution function of RMSE error changing with depth while using M-M algorithm

4.3 Discussion

In this chapter, two proposed scenarios and their RMSE results are presented. The first scenario has randomly deployed buoys and a randomly deployed target. Section 4.1 compares the RMSE between with and without using ATS. For example, using the LS method $RMSE_{before} = 14.4m$ and $RMSE_{after} = 4.4m$, the loc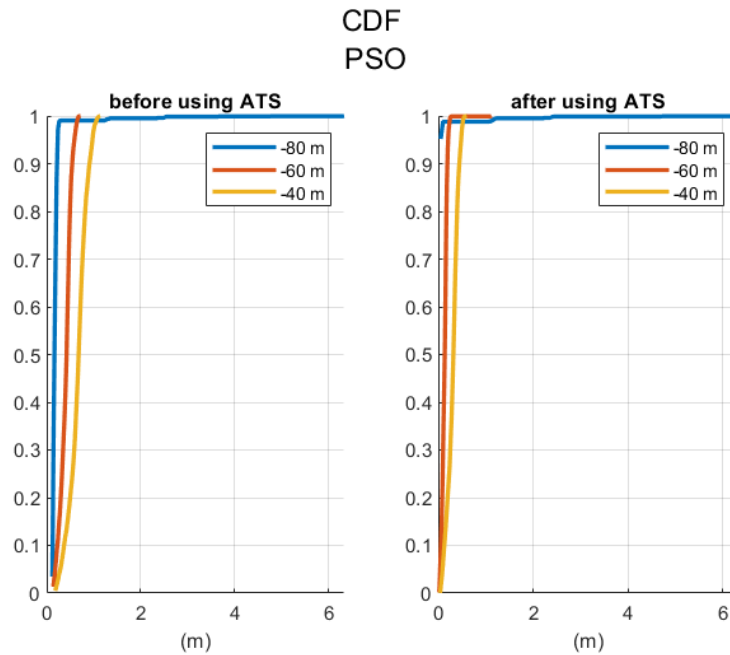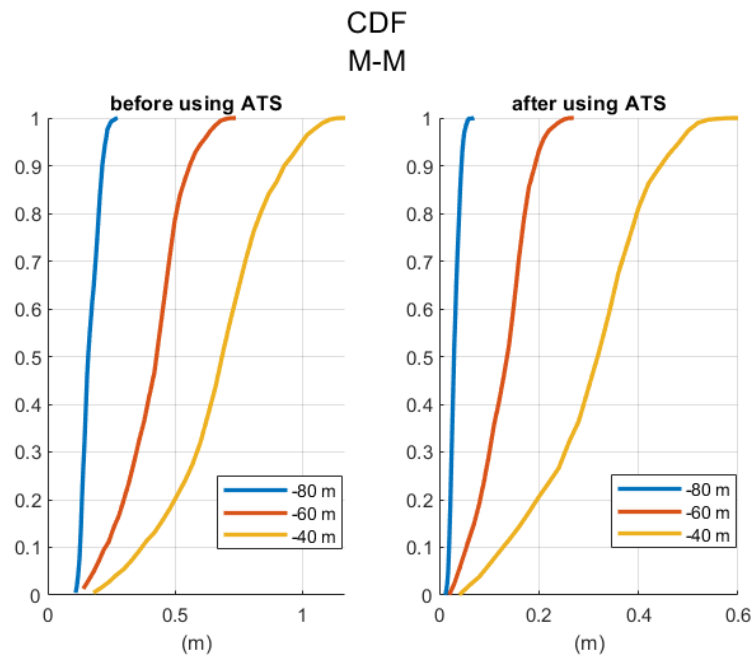alization accuracy improved by 68%, in PSO (iteration times = 100), $RMSE_{before} = 1.48m$ and $RMSE_{after} = 1.36m$, the localization accuracy improved by 8%, and in M-M approach, $RMSE_{before} = 0.28m$ and $RMSE_{after} = 0.04m$, the localization accuracy improved by 82%. In conclusion, the adaptive time slot concept improved localization reliability.

As for the second scenario described in Section 4.2, a more practical situation has been proposed, which is a 9-buoy distribution formation. The nine buoys are anchored at fixed positions. As a result, the localization accuracy of the randomly deployed target in the 9-buoy distribution scheme is slightly higher than in scenario 1. In addition, as the depth decreases, the interference from other buoys' optical signals increases, resulting in a decrease in the positioning accuracy among three localization algorithms.

However, the results presented in this thesis assume many idealistic situations. In practice, noise and interference from the outside and inside will have more influence on the positioning results, which should be considered in future work. In the assumption, the simulation area is only $100m \times 100m \times 80m$, when the ATS is used in the real setup with a larger sea area, more buoys may be required.

Chapter 5

Conclusions

This thesis introduces the background of underwater communication and the vital role of underwater optical localization in Chapter 1. The method of using the P-M spectrum to generate 3D ocean surface and the underwater optical channel properties are discussed in Chapter 2. Three typical localization algorithms are introduced at the beginning of Chapter 3. A fast underwater positioning concept, which uses adaptive time slot concept (ATS) to reduce the interference of light signals between multiple buoys, is explained in the remainder of Chapter 3. In Chapter 4, the adaptive time slot method results show better accuracy and reliability over the 10000 simulations under the two different scenarios, including randomly deployed buoy and given position scenarios. However, many assumptions are made in the simulations. The sea area is pure seawater without light scattering, no background noise or receiver noise, which should be considered in the natural environment and discussed in future work. In addition, the GPS signal received by surface buoys also has errors, which need to be taken into account as well.

Future work

In the thesis, the RSS method is used as the first stage of the underwater localization, the results of using the Time of Arrival (TOA) method can be studied. The computational complexities of different localization algorithms are not calculated, but it is also an essential factor, which should be considered in the future. Moreover, the PSO algorithm and M-M approach are only used in 2D space, and their performances can be studied in 3D space. The M-M approach uses the LS result as the initial point in the iterations. However, the PSO algorithm uses the average coordinate of all buoys, and the same initial point should be used in both algorithms to compare their results. The receiver filter is assumed to reject background noise. Different types of filters should also be considered in future work, e.g., Kalman filter.

In future work, many other analytical simulations can be carried out. For example, the water used in the simulation is pure seawater, coastal water, river water, and other types of water that should be considered. Therefore, the underwater channel will change with water type, e.g., ,the scattering effect can be formulated and added to the channel in the coastal water. The GPS errors should be taken into account, and the system should be adjusted to reduce the impact of GPS errors. Some other localization algorithms can be added to the simulations, and their performances and computational complexities can be compared. Future studies can also add the communication channel and data interaction between the buoy and the underwater target. The simulation can be carried in the experimental environment.

Bibliography

[1] N. Saeed, A. Çelik, T. Al-Naffouri, and M.-S. Alouini, "Underwater optical wireless communications, networking, and localization: A survey," *Ad Hoc Networks*, vol. 94, p. 101935, 06 2019.

[2] H.-P. Tan, R. Diamant, W. K. Seah, and M. Waldmeyer, "A survey of techniques and challenges in underwater localization," *Ocean Engineering*, vol. 38, no. 14-15, pp. 1663–1676, 2011.

[3] L. Lachman, "An open programming architecture for modeling ocean waves," *IMAGE Conference*, vol. 5, no. 7, 2007.

[4] H.-P. Yang and J.-G. Sun, "Wave simulation based on ocean wave spectrums [j]," *Acta Simulata Systematica Sinica*, vol. 9, p. 016, 2002.

[5] S. Singh, E. Mittal, *et al.*, "Range based wireless sensor node localization using PSO and BBO and its variants," in *2013 International Conference on Communication Systems and Network Technologies*, pp. 309–315, IEEE, 2013.

[6] N. Oceanic and A. Administration, "How much water is in the ocean?." `https://oceanservice.noaa.gov/facts/oceanwater.html`, accessed Feb, 2021.

[7] A. Maguer, R. Dymond, A. Grati, R. Stoner, P. Guerrini, L. Troiano, and A. Alvarez, "Ocean gliders payloads for persistent maritime surveillance and monitoring," in *2013 OCEANS - San Diego*, pp. 1–8, 2013.

[8] B. Truax, *Acoustic communication.* Greenwood Publishing Group, 2001.

[9] M. Stojanovic, "Recent advances in high-speed underwater acoustic communications," *IEEE Journal of Oceanic Engineering*, vol. 21, no. 2, pp. 125–136, 1996.

[10] A. Zielinski, Y.-H. Yoon, and L. Wu, "Performance analysis of digital acoustic communication in a shallow water channel," *IEEE Journal of Oceanic Engineering*, vol. 20, no. 4, pp. 293–299, 1995.

[11] H. Ochi, Y. Watanabe, and T. Shimura, "Basic study of underwater acoustic communication using 32-quadrature amplitude modulation," *Japanese Journal of Applied Physics*, vol. 44, no. 6S, p. 4689, 2005.

[12] H. Song and W. Hodgkiss, "Efficient use of bandwidth for underwater acoustic communication," *The Journal of the Acoustical Society of America*, vol. 134, no. 2, pp. 905–908, 2013.

[13] D. Pompili and I. F. Akyildiz, "Overview of networking protocols for underwater wireless communications," *IEEE Communications Magazine*, vol. 47, no. 1, pp. 97–102, 2009.

[14] J. Partan, J. Kurose, and B. N. Levine, "A survey of practical issues in underwater networks," *ACM SIGMOBILE Mobile Computing and Communications*

Review, vol. 11, no. 4, pp. 23–33, 2007.

[15] W. W. Au, P. E. Nachtigall, and J. L. Pawloski, "Acoustic effects of the ATOC signal (75 Hz, 195 dB) on dolphins and whales," *The Journal of the Acoustical Society of America*, vol. 101, no. 5, pp. 2973–2977, 1997.

[16] Desertstar, "Desert star systems." `http://desertstar.com/product/sam-1/`; accessed Feb, 2021.

[17] TriTech, "Tritech micron modem features." `http://www.tritech.co.uk/product/micron-data-modem`; accessed Feb, 2021.

[18] LinkQuest, "Linkquest underwater acoustic modems features." `http://link-quest.com/html/models1.htm`; accessed Feb, 2021.

[19] EvoLogics, "Evologics acoustic modems features." `http://www.evologics.de/en/products/acoustics/index.html`; accessed Feb, 2021.

[20] Teledyne, "Features of acoustic modems teledyne benthos." `http://www.f-e-t.com/images/uploads/Teledyne_Benthos`; accessed Feb, 2021.

[21] X. Che, I. Wells, G. Dickers, P. Kear, and X. Gong, "Re-evaluation of RF electromagnetic communication in underwater sensor networks," *IEEE Communications Magazine*, vol. 48, no. 12, pp. 143–151, 2010.

[22] A. I. Al-Shamma'a, A. Shaw, and S. Saman, "Propagation of electromagnetic waves at MHz frequencies through seawater," *IEEE Transactions on Antennas and Propagation*, vol. 52, no. 11, pp. 2843–2849, 2004.

[23] C. Uribe and W. Grote, "Radio communication model for underwater WSN," in *2009 3rd International Conference on New Technologies, Mobility and Security*, pp. 1–5, IEEE, 2009.

[24] R. Gabillard, P. Degauque, and J. Wait, "Subsurface electromagnetic telecommunication-a review," *IEEE Transactions on Communication Technology*, vol. 19, no. 6, pp. 1217–1228, 1971.

[25] Z. Zeng, S. Fu, H. Zhang, Y. Dong, and J. Cheng, "A survey of underwater optical wireless communications," *IEEE Communications Surveys & Tutorials*, vol. 19, no. 1, pp. 204–238, 2016.

[26] H. Singh *et al.*, "Submarine communications.," *Defence Science Journal*, vol. 43, no. 1, p. 43, 1993.

[27] A. B. Carter, J. D. Steinbruner, and C. A. Zraket, "Managing nuclear operations," 1987.

[28] S. Q. Duntley, "Light in the sea," *J. Opt. Soc. Am.*, vol. 53, pp. 214–233, Feb 1963.

[29] G. Gilbert, T. Stoner, and J. Jernigan, "Underwater experiments on the polarization, coherence, and scattering properties of a pulsed blue-green laser," in *Underwater Photo Optics I*, vol. 7, pp. 8–14, International Society for Optics and Photonics, 1966.

[30] M. Callaham, "Submarine communications," *IEEE Communications Magazine*, vol. 19, no. 6, pp. 16–25, 1981.

[31] J. J. Puschell, R. J. Giannaris, and L. Stotts, "The autonomous data optical relay experiment: first two way laser communication between an aircraft and submarine," in *[Proceedings] NTC-92: National Telesystems Conference*, pp. 14–27, IEEE, 1992.

[32] Sonardyne, "Bluecomm 200 - wireless underwater video and vehicle control." `https://www.sonardyne.com/product/bluecomm-200-wireless-underwater-video/`, 2020.

[33] M.-A. Khalighi, C. Gabriel, T. Hamza, S. Bourennane, P. Leon, and V. Rigaud, "Underwater wireless optical communication; recent advances and remaining challenges," in *2014 16th International Conference on Transparent Optical Networks (ICTON)*, pp. 1–4, IEEE, 2014.

[34] D. Toublanc, "Henyey–Greenstein and Mie phase functions in Monte Carlo radiative transfer computations," *Applied Optics*, vol. 35, no. 18, pp. 3270–3274, 1996.

[35] V. I. Haltrin, "Two-term Henyey-Greenstein light scattering phase function for seawater," in *IEEE 1999 International Geoscience and Remote Sensing Symposium. IGARSS'99 (Cat. No. 99CH36293)*, vol. 2, pp. 1423–1425, IEEE, 1999.

[36] S. Jaruwatanadilok, "Underwater wireless optical communication channel modeling and performance evaluation using vector radiative transfer theory," *IEEE Journal on Selected Areas in Communications*, vol. 26, no. 9, pp. 1620–1627, 2008.

[37] B. Tian, F. Zhang, and X. Tan, "Design and development of an led-based optical communication system for autonomous underwater robots," in *2013 IEEE/ASME International Conference on Advanced Intelligent Mechatronics*, pp. 1558–1563, IEEE, 2013.

[38] B. Cochenour, L. Mullen, and A. Laux, "Spatial and temporal dispersion in high bandwidth underwater laser communication links," in *MILCOM 2008-2008 IEEE Military Communications Conference*, pp. 1–7, IEEE, 2008.

[39] M. Doniec, C. Detweiler, I. Vasilescu, and D. Rus, "Using optical communication for remote underwater robot operation," in *2010 IEEE/RSJ International Conference on Intelligent Robots and Systems*, pp. 4017–4022, IEEE, 2010.

[40] C. Gabriel, A. Khalighi, S. Bourennane, P. Léon, and V. Rigaud, "Optical communication system for an underwater wireless sensor network," in *EGU General Assembly Conference Abstracts*, p. 2685, 2012.

[41] S. Q. Duntley, "Light in the sea," *JOSA*, vol. 53, no. 2, pp. 214–233, 1963.

[42] N. Saeed, A. Celik, T. Y. Al-Naffouri, and M.-S. Alouini, "Energy harvesting hybrid acoustic-optical underwater wireless sensor networks localization," *Sensors*, vol. 18, no. 1, p. 51, 2018.

[43] F. Akhoundi, A. Minoofar, and J. A. Salehi, "Underwater positioning system based on cellular underwater wireless optical CDMA networks," in *2017 26th Wireless and Optical Communication Conference (WOCC)*, pp. 1–3, IEEE, 2017.

[44] A. H. Sayed, A. Tarighat, and N. Khajehnouri, "Network-based wireless location: challenges faced in developing techniques for accurate wireless location information," *IEEE Signal Processing Magazine*, vol. 22, no. 4, pp. 24–40, 2005.

[45] N. Saeed, A. Celik, T. Y. Al-Naffouri, and M.-S. Alouini, "Underwater optical sensor networks localization with limited connectivity," in *2018 IEEE International Conference on Acoustics, Speech and Signal Processing (ICASSP)*, pp. 3804–3808, IEEE, 2018.

[46] N. Saeed, A. Celik, T. Y. Al-Naffouri, and M.-S. Alouini, "Robust 3d localization of underwater optical wireless sensor networks via low rank matrix completion," in *2018 IEEE 19th International Workshop on Signal Processing Advances in Wireless Communications (SPAWC)*, pp. 1–5, IEEE, 2018.

[47] N. Saeed, T. Y. Al-Naffouri, and M.-S. Alouini, "Outlier detection and optimal anchor placement for 3-D underwater optical wireless sensor network localization," *IEEE Transactions on Communications*, vol. 67, no. 1, pp. 611–622, 2018.

[48] N. Saeed, A. Celik, T. Y. Al-Naffouri, and M.-S. Alouini, "Localization of energy harvesting empowered underwater optical wireless sensor networks," *IEEE Transactions on Wireless Communications*, vol. 18, no. 5, pp. 2652–2663, 2019.

[49] Y. Noguchi, Y. Kuranaga, and T. Maki, "Adaptive navigation of a high speed

autonomous underwater vehicle using low cost sensors for low-altitude survey," in *2017 IEEE Underwater Technology (UT)*, pp. 1–4, 2017.

[50] T. Ojha and S. Misra, "Hasl: High-speed AUV-based silent localization for underwater sensor networks," in *International Conference on Heterogeneous Networking for Quality, Reliability, Security and Robustness*, pp. 128–140, Springer, 2013.

[51] P. Corke, C. Detweiler, M. Dunbabin, M. Hamilton, D. Rus, and I. Vasilescu, "Experiments with underwater robot localization and tracking," in *Proceedings 2007 IEEE International Conference on Robotics and Automation*, pp. 4556–4561, 2007.

[52] Y. Han, X. Bi, and T. Bai, "Dynamic inversion control based on backstepping for underwater high-speed vehicle," in *2010 8th World Congress on Intelligent Control and Automation*, pp. 3868–3871, 2010.

[53] I. Kirschner, J. Uhlman, and J. Perkins, "Overview of high-speed supercavitating vehicle control," in *AIAA Guidance, Navigation, and Control Conference and Exhibit*, p. 6442, 2006.

[54] L. Tartar, *An introduction to Navier-Stokes equation and oceanography*, vol. 1. Springer, 2006.

[55] M. Kass and G. Miller, "Rapid, stable fluid dynamics for computer graphics," in *Proceedings of the 17th Annual Conference on Computer Graphics and Interactive Techniques*, pp. 49–57, 1990.

[56] J. X. Chen and N. da Vitoria Lobo, "Toward interactive-rate simulation of fluids with moving obstacles using navier-stokes equations," *Graphical Models and Image Processing*, vol. 57, no. 2, pp. 107–116, 1995.

[57] S. O. Rice, "Mathematical analysis of random noise," *The Bell System Technical Journal*, vol. 23, no. 3, pp. 282–332, 1944.

[58] C. L. Bretschneider, *Wave variability and wave spectra for wind-generated gravity waves.* No. 118, The Board, 1959.

[59] W. J. Pierson Jr and L. Moskowitz, "A proposed spectral form for fully developed wind seas based on the similarity theory of SA Kitaigorodskii," *Journal of Geophysical Research*, vol. 69, no. 24, pp. 5181–5190, 1964.

[60] K. F. Hasselmann, T. P. Barnett, E. Bouws, H. Carlson, D. E. Cartwright, K. Eake, J. Euring, A. Gicnapp, D. Hasselmann, P. Kruseman, *et al.*, "Measurements of wind-wave growth and swell decay during the Joint North Sea Wave Project (JONSWAP).," *Ergaenzungsheft zur Deutschen Hydrographischen Zeitschrift, Reihe A*, 1973.

[61] O. M. Phillips, "The equilibrium range in the spectrum of wind-generated waves," *Journal of Fluid Mechanics*, vol. 4, no. 4, pp. 426–434, 1958.

[62] J. Chase and L. J. COTE, "The directional spectrum of a wind generated sea as determined from data obtained by the stereo wave observation project," tech. rep., New York Univ Bronx School of Engineering and Science, 1957.

[63] L. J. Johnson, F. Jasman, R. J. Green, and M. S. Leeson, "Recent advances in underwater optical wireless communications," *Underwater Technology*, vol. 32, no. 3, pp. 167–175, 2014.

[64] R. W. Spinrad, K. L. Carder, and M. J. Perry, *Ocean optics.* Oxford University Press, 1994.

[65] C. D. Mobley, B. Gentili, H. R. Gordon, Z. Jin, G. W. Kattawar, A. Morel, P. Reinersman, K. Stamnes, and R. H. Stavn, "Comparison of numerical models for computing underwater light fields," *Applied Optics*, vol. 32, no. 36, pp. 7484–7504, 1993.

[66] K. Shifrin, "Physical optics of ocean water, trans," *(American Institute of Physics, New York, 1988).*

[67] N. G. Jerlov, *Marine optics.* Elsevier, 1976.

[68] R. C. Smith and K. S. Baker, "Optical properties of the clearest natural waters (200–800 nm)," *Applied optics*, vol. 20, no. 2, pp. 177–184, 1981.

[69] F. E. Hoge, A. Vodacek, and N. V. Blough, "Inherent optical properties of the ocean: retrieval of the absorption coefficient of chromophoric dissolved organic matter from fluorescence measurements," *Limnology and Oceanography*, vol. 38, no. 7, pp. 1394–1402, 1993.

[70] A. Bricaud, A. Morel, and L. Prieur, "Absorption by dissolved organic matter of the sea (yellow substance) in the uv and visible domains 1," *Limnology and Oceanography*, vol. 26, no. 1, pp. 43–53, 1981.

[71] W. Breves and R. Reuter, "Bio-optical properties of gelbstoff in the Arabian Sea at the onset of the southwest monsoon," *Journal of Earth System Science*, vol. 109, no. 4, pp. 415–425, 2000.

[72] V. I. Haltrin, "Chlorophyll-based model of seawater optical properties," *Applied Optics*, vol. 38, no. 33, pp. 6826–6832, 1999.

[73] D. A. Hansell and C. A. Carlson, *Biogeochemistry of marine dissolved organic matter.* Academic Press, 2014.

[74] J. R. Apel, *Principles of ocean physics.* Academic Press, 1987.

[75] C. D. Mobley and C. D. Mobley, *Light and water: radiative transfer in natural waters.* Academic press, 1994.

[76] J. W. Giles and I. N. Bankman, "Underwater optical communications systems. part 2: basic design considerations," in *MILCOM 2005-2005 IEEE Military Communications Conference*, pp. 1700–1705, IEEE, 2005.

[77] K. S. Baker and R. C. Smith, "Bio-optical classification and model of natural waters. 2 1," *Limnology and Oceanography*, vol. 27, no. 3, pp. 500–509, 1982.

[78] J. M. Kahn and J. R. Barry, "Wireless infrared communications," *Proceedings of the IEEE*, vol. 85, no. 2, pp. 265–298, 1997.

[79] T. Hamza, M.-A. Khalighi, S. Bourennane, P. Léon, and J. Opderbecke, "Investigation of solar noise impact on the performance of underwater wireless optical communication links," *Opt. Express*, vol. 24, pp. 25832–25845, Oct 2016.

[80] H. Wang, T. Luo, H. Song, and J. B. Christen, "On-chip sensor for light direction detection," *Optics letters*, vol. 38, no. 22, pp. 4554–4557, 2013.

[81] A. S. Ghazy, S. Hranilovic, and M.-A. Khalighi, "Angular mimo for underwater wireless optical communications: Link modeling and tracking," *IEEE Journal of Oceanic Engineering*, vol. 46, no. 4, pp. 1391–1407, 2021.

[82] J. Caffery and G. L. Stuber, "Subscriber location in cdma cellular networks," *IEEE Transactions on Vehicular Technology*, vol. 47, no. 2, pp. 406–416, 1998.

[83] K. W. Cheung, H.-C. So, W.-K. Ma, and Y.-T. Chan, "Least squares algorithms for time-of-arrival-based mobile location," *IEEE Transactions on Signal Processing*, vol. 52, no. 4, pp. 1121–1130, 2004.

[84] W. H. Foy, "Position-location solutions by taylor-series estimation," *IEEE Transactions on Aerospace and Electronic Systems*, pp. 187–194, 1976.

[85] H. L. Van Trees, *Detection, estimation, and modulation theory, Part I: detection, estimation, and linear modulation theory*. John Wiley & Sons, 2004.

[86] G. Shen, R. Zetik, and R. S. Thoma, "Performance comparison of TOA and TDOA based location estimation algorithms in LOS environment," in *2008 5th Workshop on Positioning, Navigation and Communication*, pp. 71–78, IEEE, 2008.

[87] ImpactSubsea, "Isd4000 underwater depth and temperature sensor." `https://www.impactsubsea.co.uk/isd4000/`, accessed Oct, 2021.

[88] W. Cheng, A. Y. Teymorian, L. Ma, X. Cheng, X. Lu, and Z. Lu, "Underwater localization in sparse 3D acoustic sensor networks," in *IEEE INFO-COM 2008-The 27th Conference on Computer Communications*, pp. 236–240, IEEE, 2008.

[89] R. Eberhart and J. Kennedy, "A new optimizer using particle swarm theory," in *MHS'95. Proceedings of the Sixth International Symposium on Micro Machine and Human Science*, pp. 39–43, 1995.

[90] F. Marini and B. Walczak, "Particle Swarm Optimization (PSO). A tutorial," *Chemometrics and Intelligent Laboratory Systems*, vol. 149, pp. 153–165, 2015.

[91] A. Khalili, S. Akhlaghi, H. Tabassum, and D. W. K. Ng, "Joint user association and resource allocation in the uplink of heterogeneous networks," *IEEE Wireless Communications Letters*, vol. 9, no. 6, pp. 804–808, 2020.

[92] A. Beck, P. Stoica, and J. Li, "Exact and approximate solutions of source localization problems," *IEEE Transactions on Signal Processing*, vol. 56, no. 5, pp. 1770–1778, 2008.

[93] Y. Sun, P. Babu, and D. P. Palomar, "Majorization-minimization algorithms in signal processing, communications, and machine learning," *IEEE Transactions on Signal Processing*, vol. 65, no. 3, pp. 794–816, 2016.

[94] J. Smith and J. Abel, "Closed-form least-squares source location estimation from range-difference measurements," *IEEE Transactions on Acoustics, Speech, and Signal Processing*, vol. 35, no. 12, pp. 1661–1669, 1987.

[95] The Mathworks, Inc., Natick, Massachusetts, *MATLAB version 9.8.0.1323502 (R2020a)*, 2020.